University of Tennessee, Knoxville

TRACE: Tennessee Research and Creative Exchange

Masters Theses

Graduate School

8-2004

Laser-Dressing of Alumina for Grinding Wheels

Abhijeet Ashok Khangar
University of Tennessee, Knoxville

Follow this and additional works at: https://trace.tennessee.edu/utk_gradthes

Part of the Materials Science and Engineering Commons

Recommended Citation

Khangar, Abhijeet Ashok, "Laser-Dressing of Alumina for Grinding Wheels. " Master's Thesis, University of Tennessee, 2004.
https://trace.tennessee.edu/utk_gradthes/4327

This Thesis is brought to you for free and open access by the Graduate School at TRACE: Tennessee Research and Creative Exchange. It has been accepted for inclusion in Masters Theses by an authorized administrator of TRACE: Tennessee Research and Creative Exchange. For more information, please contact trace@utk.edu.

To the Graduate Council:

I am submitting herewith a thesis written by Abhijeet Ashok Khangar entitled "Laser-Dressing of Alumina for Grinding Wheels." I have examined the final electronic copy of this thesis for form and content and recommend that it be accepted in partial fulfillment of the requirements for the degree of Master of Science, with a major in Materials Science and Engineering.

Narendra B. Dahotre, Major Professor

We have read this thesis and recommend its acceptance:

Hahn Choo, Craig A. Blue

Accepted for the Council:
Carolyn R. Hodges

Vice Provost and Dean of the Graduate School

(Original signatures are on file with official student records.)

To the Graduate Council:

I am submitting herewith a thesis written by Abhijeet Ashok Khangar entitled "Laser-Dressing of Alumina for Grinding Wheels." I have examined the final electronic copy of this thesis for form and content and recommend that it be accepted in partial fulfillment of the requirements for the degree of Master of Science, with a major in Materials Science and Engineering.

Narendra B. Dahotre
Major Professor

We have read this thesis and
recommend its acceptance:

Hahn Choo

Craig A. Blue

Accepted for the Council:

Anne Mayhew

Vice Chancellor and
Dean of Graduate Studies

(Original signatures are on file with official student records.)

LASER-DRESSING OF ALUMINA FOR GRINDING WHEELS

A Thesis

Presented for the

Master of Science

Degree

The University of Tennessee, Knoxville

Abhijeet Ashok Khangar

August 2004

Dedicated to

My Family

ACKNOWLEDGEMENTS

I am very grateful to my advisor Prof. Narendra B. Dahotre for his guidance, encouragement, and support which made this work possible. I also thank Dr. Craig A. Blue and Dr. Hahn Choo for serving on the thesis committee. I thank Dr. Mark J. Jackson of the Tennessee Technological University for introducing me to this area of research. Dr. Joseph E. Spruiell's (University of Tennessee-Knoxville [UTK]), guidance in performing Pole figure analysis was very helpful. I highly appreciate the access to the orientation imaging microscopy facility at the Oak Ridge National Laboratory through the SHaRE User Center sponsored by the Division of Materials Sciences and Engineering, U.S. Department of Energy, under contract DE-AC05-00OR22725 with UT-Battelle, LLC. Dr. Edward A. Kenik and Dr. Ian M. Anderson of Oak Ridge National Laboratory were always great mentors. A special appreciation to Fred Schwartz, for his help in processing the samples. I also thank James O. Hornkohl and Newton W. Wright (Center for Laser Applications, University of Tennessee Space Institute, Tullahoma) for their help and support in the temperature measurement experiments. A special thanks to Dr. Subhadarshi Nayak (UTK) for his help. Anshul Singh, Greg Engleman and Anil Kurella (Graduate Students, UTK) were a great support during the research.

ABSTRACT

Higher the number of effective cutting edges on the surface of a grinding wheel, the higher is the grinding efficiency. However due to continuous grinding, efficiency is reduced as the effective cutting edges on wheel surface get worn out and blunt. Moreover, the wheel also gets loaded with metal chips during machining. Both geometric and functional characteristics of the grinding wheel have to be restored periodically. *Dressing* is a sharpening operation designed to generate a particular surface topography on the cutting face of the wheel. The conventional processes, like diamond dressing, do not produce consistent grinding results due to dresser wear which affects the wheel surface topography and its performance in grinding.

High power Nd:YAG laser is being explored in the present study as a non-contact type dressing tool for alumina grinding wheels. Surface processing of ceramic grinding wheels by laser irradiation offers potential advantages such as: precise control over high input of thermal energy at spatial levels, rapid processing speed and unique modification of microstructure due to rapid heating, remelting, solidification and cooling. Within the range of laser power employed, the alumina grinding wheel sample surface underwent a transformation ranging from solid-solid to liquid-solid, forming a modified layer on the surface. Refinement of the grain size took place. After laser-dressing, the individual particles on the surface evolved into defined faceted structures. Microcutting edges are generated on the individual grains and particles, which can act as cutting edges for

improved grinding. The altered grain structure on the surface of the wheel gives laser-dressing advantage over conventional mechanical methods. The surface roughness of the dressed wheel is a manifestation of the new morphologically laser modified surface and is measured using a stylus-based surface profilometric technique.

Morphological modification during laser-dressing is strongly influenced by the microstructure formed during the rapid solidification process. Microstructure in turn depends mainly on the cooling rates amongst many other factors related to the laser processing conditions. Using a two-color based optical pyrometer temperature measurement setup the cooling rates were estimated during the laser-dressing process. Orientation imaging microscopy (OIM) was used to determine the grain orientations in the resolidified layer on the dressed surface. Post laser-dressing x-ray and pole-figure analysis indicated evolution of planar crystallographic textures in the particles of the resolidified surface layer. Cooling rates and the OIM combined, indicate a preferred orientation of grains along the {110} planes. This preferred orientation can be a reason for the formation of grains with multi-faceted surfaces having cutting edges and vertices, for grinding operation. OIM and cooling results also show existence of a competitive growth mechanism for the grains in the dressed layer. Laser treatment modified the morphological features on the surface of alumina grinding wheel to achieve efficient dressing.

The performance of the laser-dressed grinding wheel was evaluated in comparison to the undressed wheel for a plain carbon steel pin using a high-speed grinding apparatus (Pin-on-disc type). The modification in morphological features on surface after laser-dressing helps maintain a very high grinding efficiency. Laser-dressed grinding wheels are best suited for efficient high-speed microscale grinding to produce smooth surface finish on the workpiece material.

There are several inherent advantages associated with the use of laser for dressing applications. Laser-dressing is a very fast process and it can be easily automated. Also, selective removal of the clogged material alone is possible and desired surface structure (roughness, grain morphology and porosity) can be generated. Furthermore, consistent dressing conditions can be produced by the use of laser and this can help achieve grinding reproducibility. As the laser beam can be delivered using a fiber optic cable, remote dressing operation without discontinuation of the grinding process, during laser-dressing is possible. Thus, the downtime in the grinding operation associated with conventional methods, can either be eliminated or substantially reduced in laser-dressing. Overall, laser-dressing can be used as an effective dressing technique.

TABLE OF CONTENTS

1. INTRODUCTION **1**

1.1 Dressing: Needs and Process 1

1.2 Grinding Wheel Wear Mechanisms 2

1.2.1 Abrasive Wear *2*

1.2.2 Fracture Wear *3*

1.3 Conventional Dressing Techniques 5

1.4 Laser as an Engineering Tool 8

1.4.1 Laser-Matter Interaction and Laser Heating *9*

1.5 Laser-Dressing: Rationale and Technique 10

1.5.1 Advantages of Laser-Dressing *11*

2. LASER INTERACTION WITH ALUMINA GRINDING WHEEL **14**

2.1 Material System 14

2.2 Laser Processing/Dressing of Grinding Wheels 15

2.3 Morphological Modifications: Macroscopic and Microscopic 19

2.3.1 Microscopic Morphological Modifications *22*

2.3.2 Compositional Modifications *24*

3. THERMAL EFFECTS **30**

3.1 Pyrometric Temperature Measurement 31

3.1.1 Principle of Two-Color Pyrometer *32*

3.1.2 Calibration of Pyrometer *32*

3.1.3 Collection Optics *33*

3.1.4 Instrumentation *34*

3.1.5 Integration of Pyrometer with the Laser Motion System *37*

3.2 Estimation of Thermal Conditions 39

4. EVOLUTION OF CRYSTALLOGRAPHIC TEXTURE 49

4.1 Bulk Surface Texture 49

4.2 Grain/Subgrain Structure 56

5. GRINDABILITY/MACHINABILITY OF LASER-DRESSED WHEELS 65

5.1 Characterization using Surface Roughness 65

5.1.1 Stylus Based Roughness Measurement Setup *65*

5.1.2 Surface Roughness Profiles *66*

5.2 High-Speed Grindability Test 69

5.2.1 Experimental Details *69*

5.2.2 Results and Discussion *71*

5.2.3 Grinding Efficiency *76*

6. CONCLUSIONS 78

REFERENCES 80

APPENDIX 86

VITA 89

LIST OF TABLES

TABLE 2.1: Chemical composition (wt %) of vitrified bonding system. **15**

TABLE 2.2: Thermophysical properties of ceramic alumina. **16**

TABLE 3.1: Cooling rate results. **40**

TABLE 3.2: G/R ratios for various processing parameters. **48**

TABLE 4.1: Qualitative comparison for the pole figure analysis at different 2θ angles for the undressed and laser-dressed samples at different powers. **52**

TABLE 5.1: Surface roughness parameters of the laser-dressed grinding wheel surface. **68**

TABLE 5.2: Surface roughness parameters of AISI 1010 plain carbon steel prior to high-speed grinding tests. **71**

TABLE 5.3: Surface roughness parameters of the AISI 1010 plain carbon steel pins after high-speed grinding testing on laser-dressed and undressed grinding wheel surfaces. **74**

TABLE 5.4: Grinding ratio for high-speed grinding testing of samples laser-dressed at varying laser power. **76**

LIST OF FIGURES

FIGURE 1.1: Process flowchart 13

FIGURE 2.1: Schematic of the laser-dressing process. 17

FIGURE 2.2: Coupons of alumina grinding wheels being laser-dressed. 18

FIGURE 2.3: Optical photographs of the grinding wheel surface (a) undressed and (b) post laser-dressed (750 W). 19

FIGURE 2.4: Macrostructure of the grinding wheel surface (a) as-received and (b) post laser-dressed (500 W). 20

FIGURE 2.5: Morphological features on a laser-dressed sample (1000 W) (a) cutting edge between faceted surfaces on a particle, (b) predominantly primary dendritic growth on the faces, (c) vertex: a point at which the cutting edges meet. 23

FIGURE 2.6: Individual particles with dendritic growth on the laser-dressed (500 W) grinding wheel surface. 25

FIGURE 2.7: Interlock bonding between adjacent particles/crystallites (a) overview (b) high magnification view. 26

FIGURE 2.8: Subsequent refinement of the grains on the surface and subsurface regions of laser-dressed (500 W) sample. 27

FIGURE 2.9: Microstructural analysis of the resolidified layer near the ridges (a) glassy surface layer and refined subsurface layer, (b) refined subsurface layer in magnified view, (c) EDS spectrum of the refined layer and, (d) EDS spectrum of the glassy layer. **28**

FIGURE 3.1: Telescope (collection optics) used with the pyrometer to collect the light intensity signal from the source. **34**

FIGURE 3.2: Schematic of the experimental setup for temperature measurement. **35**

FIGURE 3.3: Instrumentation for the optical Pyrometric temperature measurement experiment. **36**

FIGURE 3.4: Temperature vs. Time plots obtained experimentally, for two tracks on the 400 W and 500 W laser-dressed samples. **40**

FIGURE 3.5: Co-ordinates of the alumina sample during laser-dressing. The inset has one of the laser-dressed track (width ~ 3 mm) in cross-section showing the area selected for the OIM analysis. **44**

FIGURE 3.6: SEM image showing columnar growth near the edges and equiaxed grains with dendritic structure in the center of the track. **45**

FIGURE 4.1: XRD spectra of a 1000 W laser-dressed sample showing α-Al_2O_3 as the phase present. **51**

FIGURE 4.2: XRD spectra as a function of laser power for (a) (116) plane and (b) (110) plane. **51**

FIGURE 4.3: Pole figure for (116) plane in (a) undressed sample and (b) laser-dressed sample. **53**

FIGURE 4.4: Pole figure for (110) plane in (a) undressed sample and (b) laser-dressed sample. **54**

FIGURE 4.5: Pole figure for (214) plane in (a) undressed sample and (b) laser-dressed sample. **55**

FIGURE 4.6: Morphological features on a laser-dressed sample (750 W). **56**

FIGURE 4.7: Low magnification cross-sectional view of the resolidified region within a track of the 1000 W laser dressed sample. (a) SEM image and (b) Image Quality (IQ) image using OIM. **61**

FIGURE 4.8: Inverse Pole Figure (IPF) color-coded map of the selected resolidified area (in cross-section) on the laser-dressed (1000 W) grinding wheel. **63**

FIGURE 5.1: Unfiltered surface roughness profile of laser-dressed alumina samples for (a) 500 W, (b) 750 W, and (c) 1000 W. **67**

FIGURE 5.2: Schematic of high-speed grinding test apparatus. **70**

FIGURE 5.3: Cumulative weight loss in the AISI 1010 plain carbon steel pins used for high-speed grinding test of the grinding wheels. **72**

FIGURE 5.4: Unfiltered surface roughness profile of pins used for wear testing laser-dressed alumina grinding wheels for (a) undressed wheel, (b) 500 W, (c) 750 W, and (d) 1000 W. **73**

FIGURE 5.5: Surface topography of pins ground against (a) undressed wheel and (b) laser-dressed wheel at 1000 W. **75**

FIGURE A.1: (a) Laser-dressed grinding wheel showing pyramidal grains (grits), and (b) approximation of the grit as a pyramidal indenter. **87**

LIST OF SYMBOLS

α	Attack angle of grit
ρ	Density (kg/m^3)
κ	Shear yield strength of the work surface
κ_s	Thermal conductivity of substrate (W/mK)
μ	Force ratio (F'_t / F'_n)
μ_o	Coefficient of friction on the grit rake interface
τ_l	Laser beam dwell time (s)
C_p	Specific heat at constant pressure (J kg^{-1} K^{-1})
d	Scratch depth
D	Thermal diffusivity (m^2/s)
f_n	Normal force on the grit
F'_t	Specific tangential force
F'_n	Specific normal force
G	Thermal gradient (°C/m)
H_s	Microhardness of the work surface (MPa)
H_b	Bulk hardness of work surface (MPa)
ΔH_m	Latent heat of fusion (J/kg)
I_a	Absorbed laser beam intensity (W/m^2)
K	Abrasive wear coefficient (MPa^{-1})

l	Relative overlap (overlap/scratch width) of successive grinding scratches
l_a	Geometric length of arc of cut
n_g	Number of grits per unit area
$\dot{q}$	Extra heat term (e.g.: latent heat, etc.)
R	Growth rate (m/s)
R_a	Arithmetic mean roughness
R_{max}	Maximum roughness depth
RP_c	Peak Count
R_z	Average maximum height
t_0	Time at which data acquisition starts during temperature measurement (s)
t	Time during solidification (s)
T	Temperature (K)
T_m	Melting temperature (K)
T_o	Initial temperature (K)
v	Laser beam travel velocity (m/s)
V_i	Liquid/solid interface velocity (m/s)
V_s	Wheel speed (m/s)
y	Distance in melt pool
Z'	Specific metal removal rates
Z_g	Metal removal rate per grit

ABBREVIATIONS

CBN	Cubic Boron Nitride
EDM	Electrical Discharge Machining
EDS	Energy Dispersive X-ray Spectroscopy
ELID	Electrolytic In-process Dressing
LASER	Light Amplification by Stimulated Emission of Radiation
Nd:YAG	Neodymium:Yttrium/Aluminum/Garnet (Laser)
OIM	Orientation Imaging Microscopy
SEM	Scanning Electron Microscopy
XRD	X-ray Diffraction

1. INTRODUCTION

1.1 Dressing: Needs and Process

Grinding is a manufacturing process used to achieve the desired surface finish on the material. It is an important process as it makes possible strict tolerances, thus making it a widely used industrial technique. Superabrasive wheels such as diamond, cubic boron nitride (CBN), are used for grinding materials with poor machinability because of their longer life, high grinding efficiency, and dimensional stability [1]. Alumina ceramics offer great potential as materials for tribologically loaded parts owing to their unique combination of low weight, high stiffness, strength, temperature stability, and corrosion resistance.

Whilst grinding wheels are significantly harder than the workpiece, some wear does occur; this reduces process efficiency, accuracy and quality of surface finish. Due to wear or attrition during continuous grinding operations, the number of effective cutting edges on the wheel surface is reduced causing a decrease in grinding efficiency. Thus the grinding wheel needs to be dressed to maintain its form tolerance and dimensional stability over a large number of grinding passes. The wheel also needs to be cleaned of the clogged metal chip particles that get loaded into the grinding wheel surface during the grinding operation [2, 3].

Ideally, the abrasive particles on the surface of the grinding wheel should get automatically sharpened when worn out, by either entirely detaching from the wheel face or by fracture, thus exposing new particles with sharper cutting edges. However, in practice both geometric and functional characteristics of the grinding wheel have to be restored periodically by dressing . *Dressing* is a sharpening operation designed to generate a particular surface topography on the cutting face of the wheel. Dressing of the worn out grinding wheel surface is done by various means to modify its surface topography, which in turn strongly influences the wheel performance and improves the grinding efficiency .

1.2 Grinding Wheel Wear Mechanisms

Four distinct wear mechanisms that contribute to the wear of grinding wheels are:

1. Abrasive wear (formation of wear flats on the surface of abrasive grains).
2. Fracture of bond bridges.
3. Fracture of abrasive grains due to mechanical and thermal shock loads.
4. Fracture at the interface between abrasive grain and bond-bridge.

1.2.1 Abrasive Wear

The formation of wear flats on the abrasive grains leads to a loss of grain sharpness. The sources of wear are:

a. Wear due to frictional interaction between workpiece and abrasive grain.

b. Plastic flow of the abrasive grain at the high temperature and pressure.

c. Crumbling of the abrasive grain due to thermal and microscale mechanical impact.

d. Chemical reaction between abrasive and workpiece material at elevated temperatures and in the presence of grinding fluids.

Dull abrasive grains are caused by the generation of wear flats on the active grains that leads to an increase in the area of contact and by frictional interaction between the abrasive grain and workpiece. At the point where the abrasive grain dulls, very high temperatures exist in the area of contact that greatly enhances adhesion and chemical reaction between the two surfaces. If grain and bond bridge fracture does not occur during grinding then the plateau area on the grain widens and the rate of wear increases. If fracture is delayed further, as with hard grinding wheels, then the wheel becomes glazed and the workpiece is thermally damaged.

1.2.2 Fracture Wear

The occurrence of abrasive grain and bond fracture are considered simultaneously for the following reasons:

a. They are of the same nature, i.e. fracture of brittle-type materials and hence the theory of brittle fracture is applicable to both bonding bridge and abrasive grain. The applied thermal and mechanical loads, usually under cyclic conditions, cause initiation and further developments of cracks that leads to fracture and the

formation of new irregular surfaces.

b. They are related to dressing methods used and occur simultaneously. The initial and final stages of wheel life between dressing, exhibit fracture wear that is the combination of abrasive grain and bonding bridge fracture.

c. The relative amounts of bond bridge and abrasive grain wear cannot always be calculated.

Combination of grinding parameters such as equivalent chip thickness and the grindability of the workpiece material determine the effective wheel hardness, and so no single feature of the grinding process can be used to predict the fracture pattern of the wheel in advance. The difficulty when relating the grinding wheel wear due to fracture to a particular grinding condition arises from the lack of knowledge about the loads applied to both abrasive grains and their bonding bridges and their response to these applied loads.

Although bond and grain fracture are similar mechanisms, they have a different effect on the economics of the process. The first mechanism results in rapid loss of grinding wheel, while the second mechanism, on a comparable scale with the un-cut chip thickness, generates sharp cutting edges and is known as 'self-dressing action'. The effect of heat at the abrasive grain and workpiece interface is responsible for locally affecting the mechanical properties of the abrasive grain.

1.3 Conventional Dressing Techniques

In order to optimize the wheel preparation process, the following requirements should be adhered to:

- Bonding material should be removed evenly in every direction surrounding the abrasive grain.
- Grain protrusion heights of abrasive grains should be controlled so that the optimum range for various workpiece materials is achieved.
- Grinding wheels should be dressed on the grinding machine to prevent loss of concentricity.
- Bond material should be removed evenly throughout the whole of the working area of the grinding wheel surface to prevent grinding instability and chatter.

To achieve these requirements, methods have been developed to maintain an optimized grinding wheel. These methods include: slurry and steel roll application, pressurized jet dressing using abrasive slurry, and air jet abrasive dressing. In air jet dressing, the dressing rate is controlled in three ways: (a) by controlling the pressure of the mixed air; (b) by controlling the ejecting abrasive traverse speed; and (c) by controlling the number of traverse passes across the grinding wheel. Therefore, the dressing rate will control the optimum grain protrusion height.

Prior to any dressing operation, the grinding wheel tends to load with metal chips that

need to be removed. Wheel loading is one of the most common problems in grinding operations. As grinding continues, removed chips may adhere in the spaces between abrasive grains and deteriorate the cutting ability of the grinding wheel. A common method used to prevent the wheel from loading is by delivering a large amount of coolant to the grinding zone. However, this consumes huge amounts of energy in coolant delivery, especially for high speed grinding processes. Maintaining and disposing of coolant is also an environmental issue and the costs involved are substantial. Another method, which is often used, is to remove loaded chip materials by dressing the wheel periodically, to restore a sharp wheel surface. However dressing of grinding wheels with diamond not only causes excessive wheel loss but also interrupts grinding during dressing. In addition, the dresser wears away with time due to its direct contact with the wheel surface. Frequent use of dressing wheels is also not acceptable for super-abrasive wheels whose cost is considerably more than conventional grinding wheels.

Dressing significantly affects the quality of the ground product, as characterized by its size and shape, surface roughness and integrity . The conventional contact-type methods, like mechanical dressing using a diamond dresser, result in excessive grinding wheel material loss. The bond fracture and abrasive grain break-off, as a result of crushing of the dresser are the material removal mechanisms for these contact type processes. In fact, only 10 percent of the wheel by volume is removed during actual grinding, while the rest is removed during dressing operations . Mechanical dressing, though effective, also

induces stresses and causes deep cracks and undercuts. These factors eventually cause loosening of the chunks of grains and reduce the number of effective cutting edges .

The conventional processes do not produce consistent grinding results due to dresser wear which affects the wheel surface topography and its performance in grinding. A worn-out dresser cannot produce sufficient protrusion of cutting grain edges . To obtain consistent grinding outputs, either the dresser geometry has to be maintained or suitable dressing conditions corresponding to modified dresser geometry have to be selected, which are impossible in contact type processes and also complicated because of dresser wear . Yet in order to obtain consistent grinding results, a dressing procedure, which is reproducible in nature, is essential.

Electrical discharge machining (EDM) dressing [4] and electrolytic in-process dressing (ELID) are some of the other dressing techniques in use. The ELID process [5, 6] makes use of the electrolytic effect to remove the bonding material (metallic or resin-metallic) from the wheel surface. The conventional processes such as mechanical diamond dressing result in excessive wheel material loss and also reduce the number of effective cutting edges present on the surface of the wheel, thus reducing the efficiency of the grinding process [7, 8]. In the light of this, high power lasers that are currently used as an efficient non-contact type machining tool for various manufacturing applications like cutting, drilling, welding etc., have also been explored as a dressing tool [1, 2, 8, 9].

1.4 Laser as an Engineering Tool

Laser is acronym for "Light Amplification by Stimulated Emission of Radiation". Laser works on the principle of exciting atoms to a high-energy state level and then to get an inversion in population with respect to an intermediate level. When radiation interacts with the excited atom with a frequency that corresponds to the energy difference between the higher energy state of the atoms and the intermediate state with inverted population, it produces an emission of radiation with the same phase as the incidental radiation. It is possible to amplify this radiation by using a resonance cavity, in order to get a beam of coherent light. Besides its coherence, the emitted light is highly monochromatic which enables efficient focusing. A laser can be used to heat or melt material locally. The coherent nature of the laser beam allows it to be focused to a small spot, leading to high energy density [10]. This property of laser makes possible very small spot sizes. Thus, a very high intensity (up to 10^{10} W/m2) can be attained. The medium used for laser determines the wavelength and quality of laser. The primary lasers available in market for high power applications are continuous-wave CO_2 laser (wavelength 10.6μm), Nd:YAG laser (active entity Nd^{+3} with wavelength 1.06 μm) and excimer (lasing medium dimer-a compound between is one inert gas atom and a halide atom, wavelength in ArF: 193 nm, KrF: 248 nm, XeCl: 308 nm and XeF: 351 nm). Nd:YAG lasers have gained popularity primarily for the flexibility provided by fiber optical beam delivery making it suitable for many applications.

1.4.1 Laser-Matter Interaction and Laser Heating

The input of energy from pulsed/continuous wave lasers into the near-surface regions of a solid material involves electronic excitation and de-excitation within an extremely short period of time. The interest in these energy deposition techniques arises as lasers can be used to achieve extreme heating and cooling rates in the near-surface region, while the total deposited energy is insufficient to affect, in a significant way, the temperature of the bulk material. This allows the near-surface region to be processed under extreme conditions with little effect on bulk properties. The initial stage in all laser-material processing applications involves the coupling of laser radiation to electrons within the metal. This first occurs by the absorption of photons from the incident laser beam promoting electrons within the material to higher energy states. Electrons that have been excited in this manner can divest themselves of their excess energy in a variety of ways. For example, if the photon is energetic enough, excited electrons can be removed entirely from the metal. This is the photo-electric effect, and in most materials, requires photon energies greater than several electron volts. However, the laser photons have usually much less energy (CO_2 laser 0.12 eV and Nd:YAG laser 1.2 eV). Hence, the electrons that have absorbed energy from laser photon may not be energetic enough to leave the material, but they do have to lose energy to get back to ground state. This occurs when excited electrons are scattered by lattice defects. Such defects can be dislocation, grain boundary, lattice distortion (due to photon, thermal or other kind of stress). Consequently, the photon energy is converted to thermal energy. Photon interactions with matter occur usually through the excitation of valence and conduction band electrons throughout the

wavelength band from infrared to ultraviolet region. Since, free carrier absorption by conduction band electrons is the primary route of energy absorption on materials, beam energy is almost instantaneously transferred to the lattice by electron-photon interaction. Interaction of laser beam at electron level provides tremendous control over thermal processing of materials in very confined region for applications such as cutting, joining, drilling, dressing etc.

1.5 Laser-Dressing: Rationale and Technique

High power lasers are currently used as an efficient non-contact type machining tool for various manufacturing applications like cutting, drilling, welding etc. It has also been explored as a dressing tool [1, 2, 7]. Laser is an efficient tool to process ceramic materials because of its high intensity and directionality. Laser-dressing can be performed on a grinding wheel to generate surfaces with sharp cutting edges, either by locally modifying the worn-out particles and/or by dislodging the loaded metal chips. Focused laser radiation produces enormous power densities in a very small region of the wheel surface and thus can cause a localized modification either of the exposed grain or of the bond. Since the focused spot size can be made much smaller compared to nominal size of the abrasive grain, it can pierce through abrasive grain and produce multiple cutting edges on the same grain.

1.5.1 Advantages of Laser-Dressing

The application of laser in the dressing of grinding wheels has the following merits:

- A very narrow zone of material is processed thus producing a narrow kerf and saving the grinding wheel material.
- Laser-dressing is a fast process and can be easily automated.
- Selective removal of clogged material alone is possible.
- Laser-dressing being a non-contact type process, there is no dressing tool wear and it is possible to obtain grinding reproducibility with reproducible dressing conditions.
- The loss of grinding wheel material is negligible as compared to mechanical dressing.
- Presence of the normal cooling films may not affect the dressing process.
- Remote dressing operations are possible due to non-contact nature of laser-dressing.
- In-situ and/or simultaneous dressing can be performed during grinding operation.

Earlier studies [2, 7, 11, 12, 13] used pulse laser to compare the laser-dressing process with conventional mechanical dressing methods. The pulsed laser powers used were of the order of 1-5 x 10^{10} W/m^2 and most of the work concentrated on comparison of the grinding performance of laser-dressed wheels with that of diamond-dressed ones. Laser-assisted simultaneous truing and dressing has also been attempted, to overcome the problems associated with mechanical dressing . Though useful, the studies did not deal with the nature of physical changes taking place in the grinding wheel during interaction with laser energy, which happens to be a fundamental aspect to contribute towards its dressing performance.

The present work therefore has attempted to study and provide insight into physical and crystallographic changes taking place during laser-dressing of grinding wheels. In light of this, the process flowsheet for the approach adopted during the experimentation and analysis of the results during laser-dressing is given in Figure 1.1.

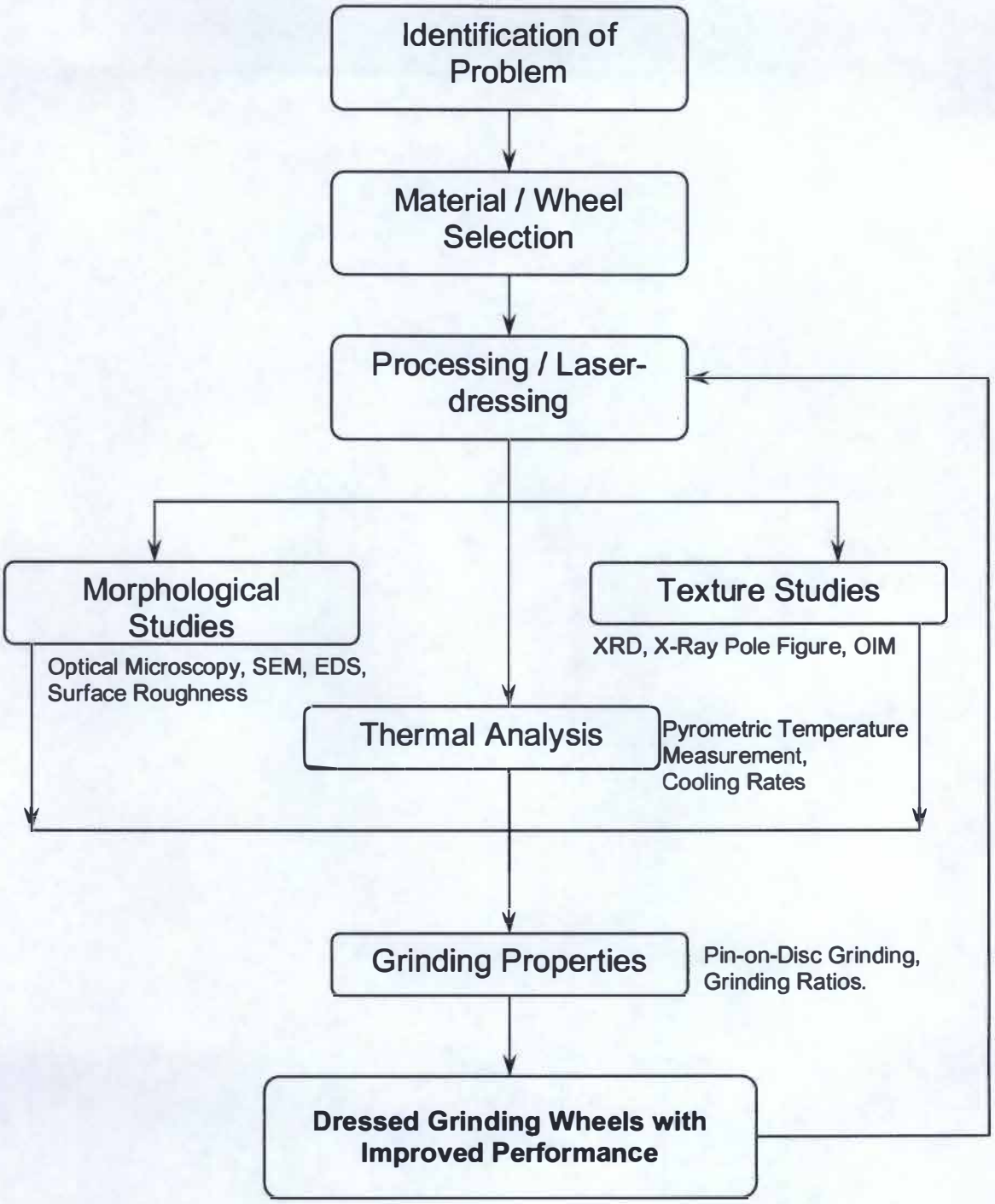

FIGURE 1.1: Process flowchart.

2. LASER INTERACTION WITH ALUMINA GRINDING WHEEL

When lasers are used as a heat source for dressing grinding wheels, a very high input of energy is concentrated in a very small region on the surface. Thus, the focused laser radiation produces enormous power densities in a very small region of the wheel surface. This chapter describes the morphological changes taking place on the surface of the grinding wheel during interaction with such high density laser energy.

2.1 Material System

Chromium doped alumina is selected as the abrasive grain material as it is commonly used for grinding tough engineering materials such as microalloyed steels, and is used in a wide variety of industrial applications such as roll, camshaft, and crankshaft grinding, and in other automotive component grinding operations. The chemical composition of the abrasive grain material in the grinding wheel is 99.52 Al_2O_3 – 0.05 Fe_2O_3 – 0.18 Na_2O – 0.25 Cr_2O_3 (wt %). The abrasive grains were bonded into a cylindrical grinding wheel by mixing with a vitrified bonding system. Vitrified bonds are composed of glasses that are formed when clays, ground glass frits, mineral fluxes such as feldspar, and chemical fluxes such as borax melt when the grinding wheel is fired at high temperatures. The grains were coated in dextrin and mixed with water to form a sticky, wet mass. The mass

of bonding ingredients was pressed to shape at a predetermined density such that a porosity level of about 40 vol. % was achieved. The batch composition of the bond (wt %) was 14% ball clay, 11 % bentonite clay, 17.5 % potassium feldspar, and 57.5 % borax. Chemical composition is as given in Table 2.1. After firing of the bond constituents in a high temperature furnace, the wheels obtained were of K grade (medium hardness), 6 structure (relatively open wheel), and possessed a single grain size of approximately 220 μm diameter (60 mesh). The relative proportions of grain, bonding system, and porosity were 50, 9.5, and 40.5 % by volume respectively. Some of the thermophysical properties of alumina in the grain material of grinding wheel are given in Table 2.2.

2.2 Laser Processing/Dressing of Grinding Wheels

A 2.5 kW Hobart continuous wave Nd:YAG laser equipped with a fiber-optic beam delivery system was used for dressing Al_2O_3 grinding wheel. The lenses within the output-coupling module of the fiber optic delivery system were configured to provide a

TABLE 2.1: Chemical composition (wt %) of vitrified bonding system.

SiO_2	Al_2O_3	Fe_2O_3	TiO_2	CaO	MgO	Na_2O	K_2O	B_2O_3
71·53	13·48	0·45	0·20	0·61	0·43	4·36	3·79	5·15

TABLE 2.2: Thermophysical properties of ceramic alumina.

Property	Value*
D - thermal diffusivity (m^2/s)	1.24×10^{-6}
ΔH_m - latent heat of fusion (J/mol)	1.049×10^{6}
T_m - melting temperature (°K)	2323
ρ - density (Kg/m^3)	3.848×10^{3}
C_p - specific heat (J/Kg°K) $C_p(Al_2O_3) = 117.49 + (10.38 \times 10^{-3})\,T - \left(\frac{37.11\times10^{-5}}{T^2}\right)$ J /mol°K	1389
* Source: http://www.ceramics.nist.gov/srd/summary/scdaos.htm	

3.5 mm × 600 μm rectangular beam in spatial distribution onto the sample surface. Such configuration provides rapid processing speed and limits the overlap between the laser passes to less than 20%. Laser power intensities of 400, 500, 750 and 1000 W (average power densities of 19×10^9, 24×10^9, 36×10^9, 48×10^9 W/m^2 respectively) were employed. Dressing of the entire surface was done by scanning the laser beam in parallel tracks at a linear speed of 250 cm/min on the surface, as shown in the schematic in Figure 2.1. The actual processing at first was done on small coupons of the alumina grinding wheel (Figure 2.2). A slow speed diamond laced wheel was used for stress-free cutting of the dressed wheel samples for further characterization. Microstructural analysis was done using Scanning Electron Microscopy (SEM). To minimize charging during SEM, low vacuum (~ 30 Pa air) was maintained in the SEM chamber.

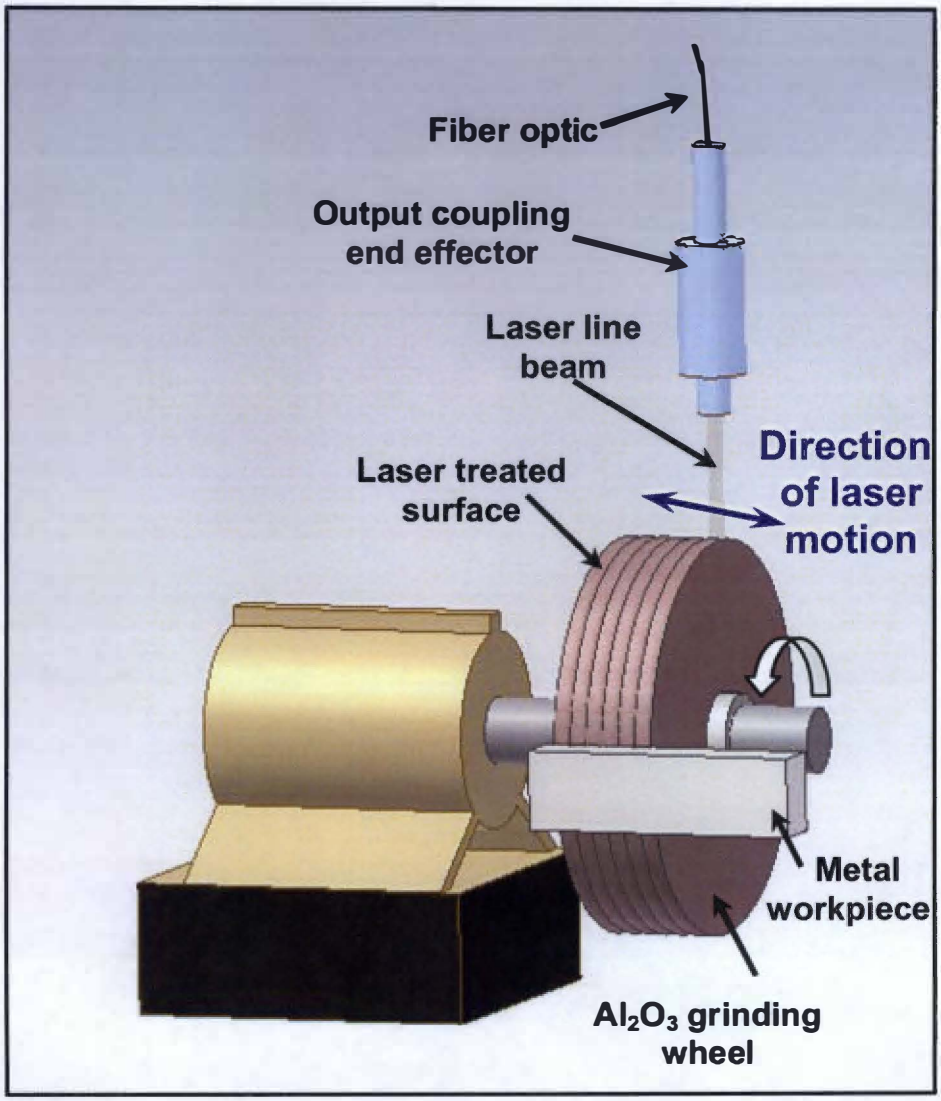

FIGURE 2.1: Schematic of the laser-dressing process.

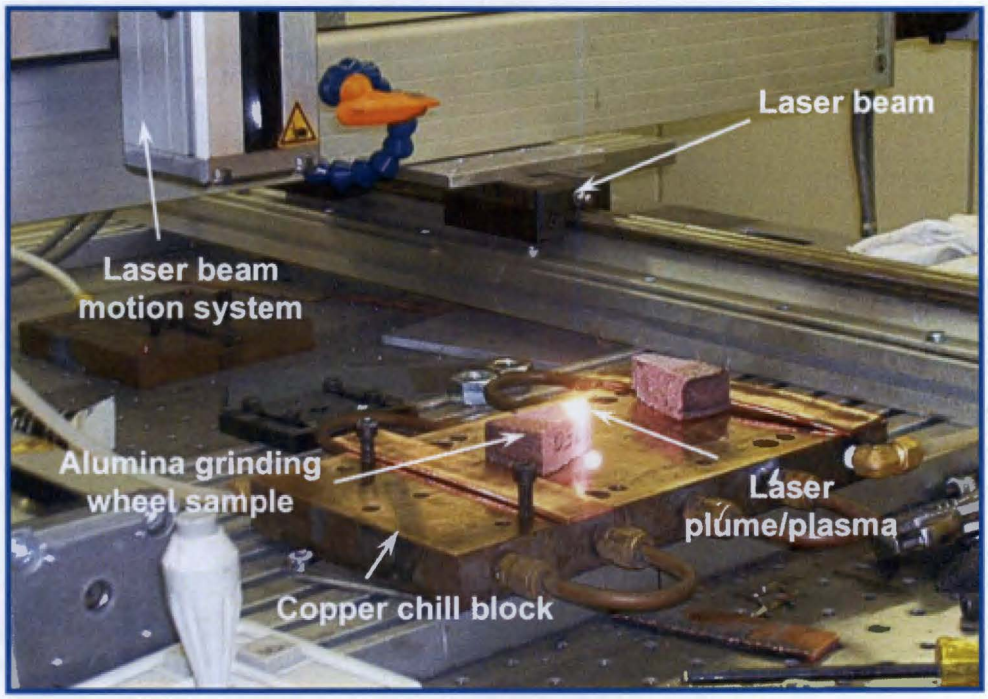

FIGURE 2.2: Coupons of alumina grinding wheels being laser-dressed.

2.3 Morphological Modifications: Macroscopic and Microscopic

Overview of the undressed (as-received) surface is shown in Figure 2.3a and that of the laser-dressed surface in Figure 2.3b. Furthermore, at this higher magnification surface structure of the as-received grinding wheel is illustrated in Figure 2.4a and that of the dressed surface in Figure 2.4b. The as-received wheel surface has relatively large particles (100 – 150 μm) with considerable porosity in between. The particles are irregular in shape with a few bonding bridges between them. The addition of Cr_2O_3 gives the grinding wheel its characteristic pink color. Within the range of laser power employed, the sample surface underwent a transformation ranging from solid-solid to liquid-solid. Depending upon the laser processing parameters used, the high thermal energy produced during laser processing caused melting and/or vaporization of the grinding wheel material on surface.

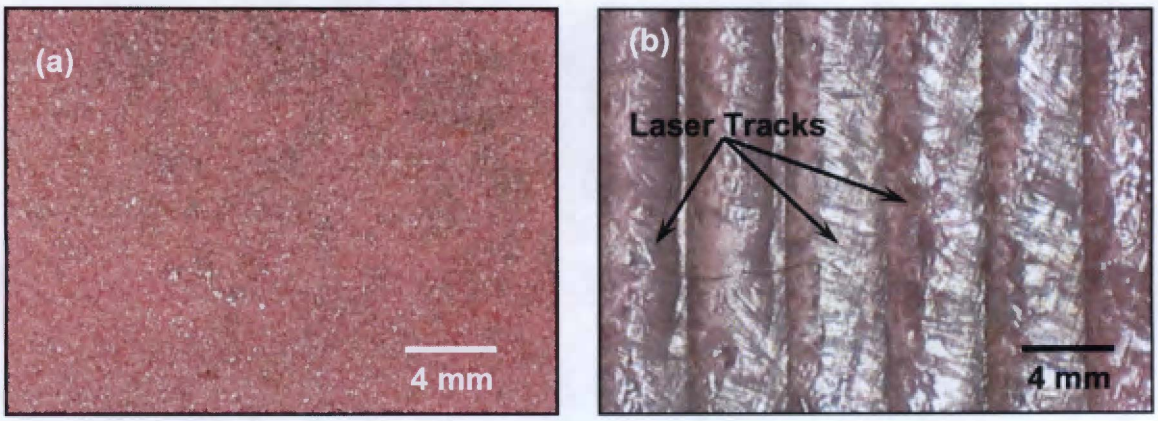

FIGURE 2.3: Optical photographs of the grinding wheel surface (a) undressed and (b) post laser-dressed (750 W).

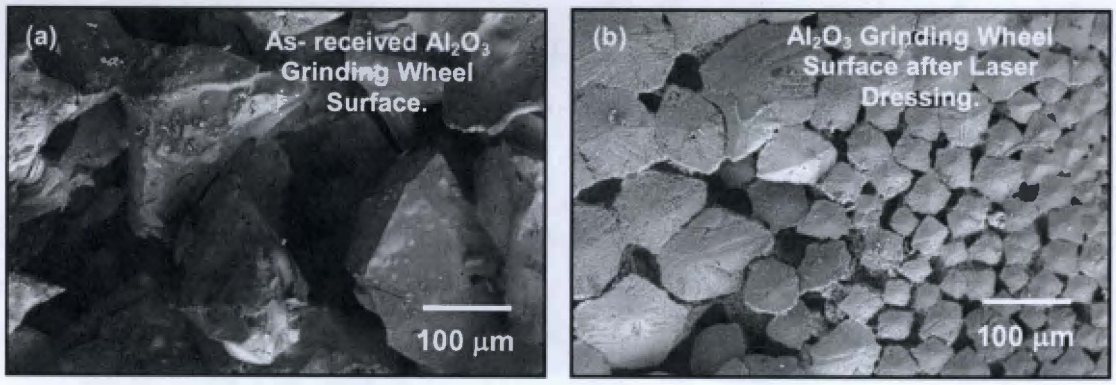

FIGURE 2.4: Macrostructure of the grinding wheel surface (a) as-received and (b) post laser-dressed (500 W).

Thus, both melting (followed by resolidification) and/or vaporization resulted in modification of surface topography (morphology and composition). The melted material resolidifies very fast, as a layer on the surface. This resolidified layer has a distinct luster as compared to undressed material. Using different laser processing parameters (beam focus, power and transverse speed); the extent of the modified layer on the surface can be controlled for various surface topographies. Laser-dressing also ablated the bond material, as these are generally low temperature melting compounds such as Na_2O and K_2O (melting temperatures ~ 800-900 ^{0}C as compared to 2050 ^{0}C of alumina). With properly selected heating time and energy density, the vitrified bond (glass phase) of the wheel gets softened and even melted, thus facilitating the removal of the bonding material . Dressing of the grinding wheel by laser generated well-defined grooves/tracks on the wheel surface. Microstructural analysis also revealed microcracks and refinement of the grain structure.

During the dressing process, rapid heating and cooling induced microcracks in the re-solidified layer as a result of the associated high thermal stresses, caused by the steep temperature gradient across the sample surface due to poor thermal conductivity of the ceramic (Al_2O_3). Also, overlapping of the adjacent tracks induced stresses and formed microcracks in the resolidified layer on the near-ridge (laser track overlap) region of the surface. When these cracks are formed on the bond, the particles are loosened and subsequently removed due to insufficient volume for load surrounding the grain [2]. For the higher laser powers of 750 and 1000W, the resolidified layer on the surface is observed to be smooth, dense and covering the entire dressed region, where as for the very low (< 500 W) laser powers dressed sample, though the refinement in the microstructure was observed in the dressed regions, the laser power was sufficient enough, only to melt a small fraction of the material on the surface. In other areas, an increase in the bridge bonding between the particles originally present in undressed wheel was observed. After laser dressing, densification of the surface layer occurred. Similar observations were made in studies where refractory materials were treated with laser [14, 15, 16].

Although, laser-dressing reduced the porosity for increased densification within the surface, such a feature is desired in the grinding wheel. Due to the presence of optimum amounts of porosity, unsupported particles at the surface of wheel break away once worn out during grinding, thereby leaving the remaining particles with sharp edges. These morphological changes can help to maintain a high grinding efficiency and low grinding wheel material loss at all the times. Also, an optimum amount of porosity is desired in

between the particles to accommodate the metal chips removed from the workpiece during the grinding operation.

2.3.1 Microscopic Morphological Modifications

Laser-dressing produced microcutting edges on the worn out grains in the wheel. Particles in the newly formed resolidified layer were of modified geometry and are characterized by multi-faceted surfaces. Though a wide distribution on sizes of the particles (5-100 μm) was seen, the shape of the particles was more regular and symmetric with well-defined vertices and edges on each particle. The wide distribution of size helps achieve a surface with higher packing fraction. Moreover it can help to achieve a smoother worksurface finish during grinding operation. The vertices and edges are expected to provide cutting edges for improved grinding efficiency. Figure 2.5 shows one such multifaceted particle on the surface of the sample. Change in the direction of the dendritic growth can be observed across the cutting edges and the vertex. Laser being a high-energy density source, dressing was conducted at a high speed, resulting in rapid solidification of the melted material on the surface. Under such rapid solidification conditions, predominantly primary dendritic growth was observed on the particles.

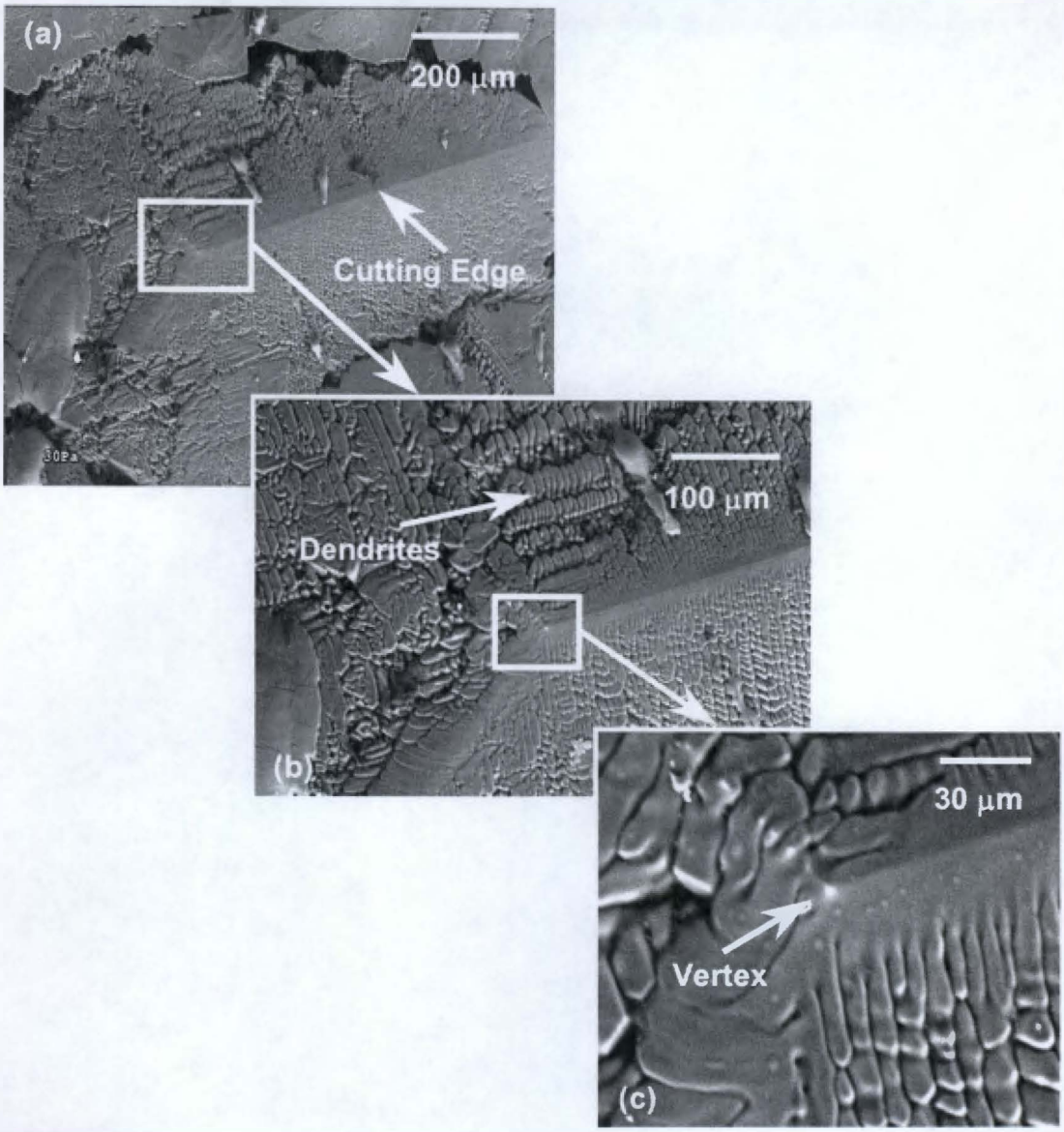

FIGURE 2.5: Morphological features on a laser-dressed sample (1000 W) (a) cutting edge between faceted surfaces on a particle, (b) predominantly primary dendritic growth on the faces, (c) vertex: a point at which the cutting edges meet.

The dendritic growth that has taken place on the individual particles in all directions, is illustrated in Figure 2.6. A large variation in the shape of the dendrites was seen. Formation of similar particles has been reported in refractory systems when laser treated [14, 16, 17]. The particles are held together by grains which are much smaller and cubic in shape. This is in contrast to the brittle bond phases in the as-received wheel. Thus the cubic grains interlock to form mechanical bonding between the adjacent particles on the surface in the laser-dressed wheel. Such an interlocking between the particles is seen in Figure 2.7.

The refinement in the microstructure due to laser-dressing is a characteristic feature of the surface and subsurface region, as shown in Figure 2.8. The microstructure obtained during solidification, depends on the temperature gradient and the solidification rate. The temperature gradient to the solidification rate ratio controls the type of structure obtained, and an increase in this ratio causes a change in the solidification growth front from dendritic to cellular to planar [18]. Also, the size of the microstructural features depends on the cooling rate. During laser processing, the interaction region between the laser beam and the sample surface is very small and the cooling rate is very high, thus resulting in refinement of the microstructure on surface.

2.3.2 Compositional Modifications

Energy Dispersive Spectroscopy (EDS) gives partially resolved chemical composition of the sample. The EDS signal comes from the volume of matter excited by an electron

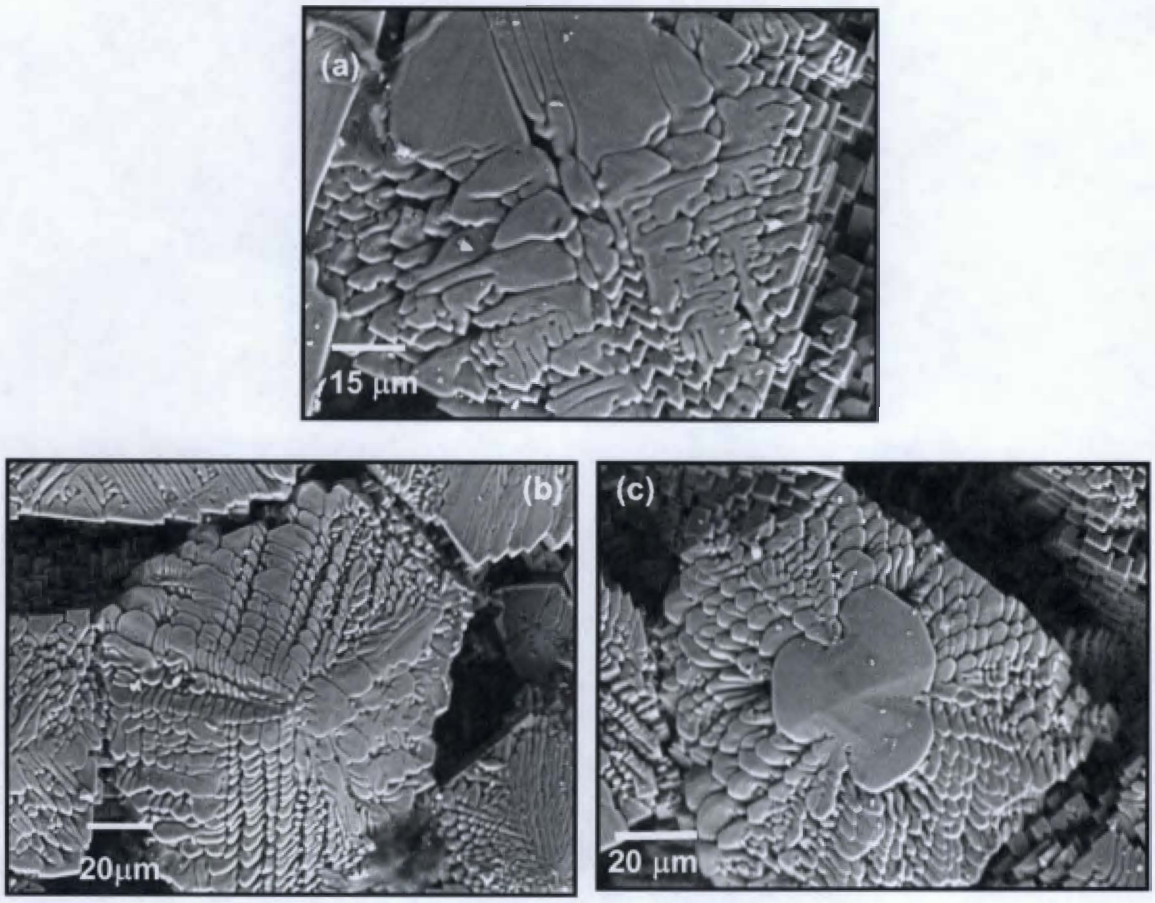

FIGURE 2.6: Individual particles with dendritic growth on the laser-dressed (500 W) grinding wheel surface.

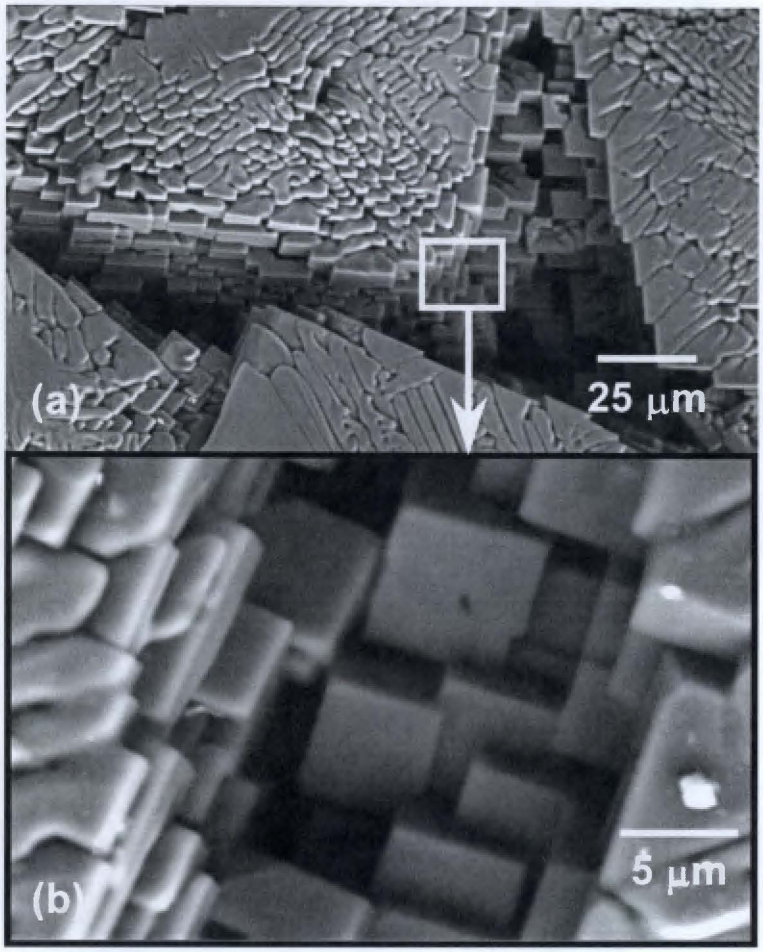

FIGURE 2.7: Interlock bonding between adjacent particles/crystallites

(a) overview (b) high magnification view.

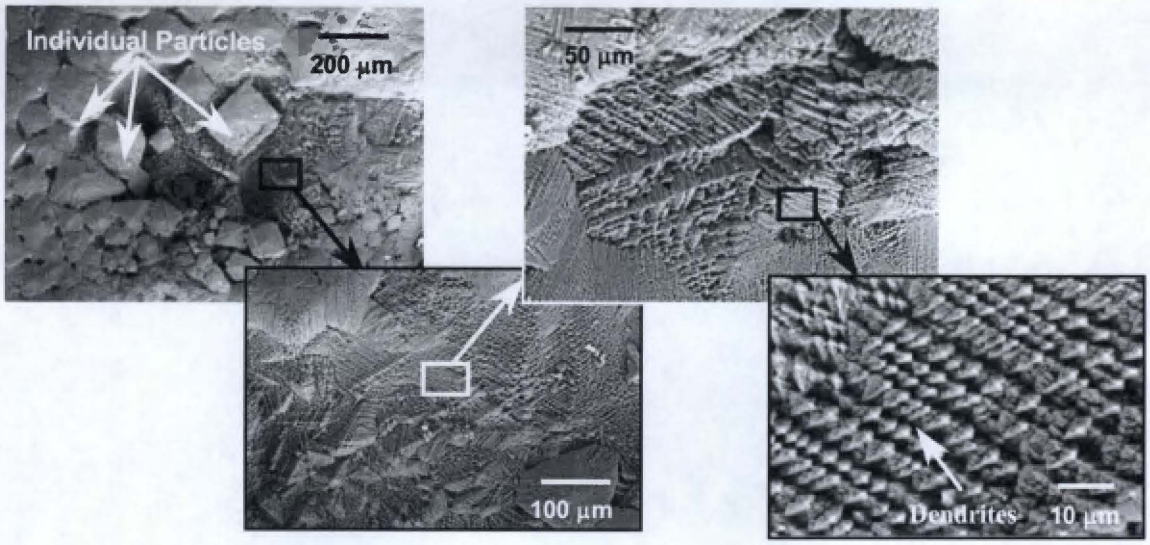

FIGURE 2.8: Subsequent refinement of the grains on the surface and subsurface regions of laser-dressed (500 W) sample.

beam. By choosing an appropriate low voltage (LV), it is possible to analyze microstructural features with high resolution using EDS.

Area analysis by Energy Dispersive Spectroscopy (EDS) revealed the presence of Al, Cr, O, Si, K and Na (Figure 2.9). Cr, Si, K, P and Na, contributed by additions (Cr-oxide) to abrasive grain material and by the vitrified bond phase, were present either in solid solution with Al_2O_3 or in a glassy phase. The upper resolidified layer in the near-ridge (laser track overlap) region contained Si, Na, K and P whereas the material beneath it was primarily Al, Cr and O (Figure 2.9c and 2.9d). This observation in conjunction with microstructural studies suggests segregation of Na, K, P and Si in a glassy top-resolidified layer in the near-ridge (laser track overlap) region of the surface.

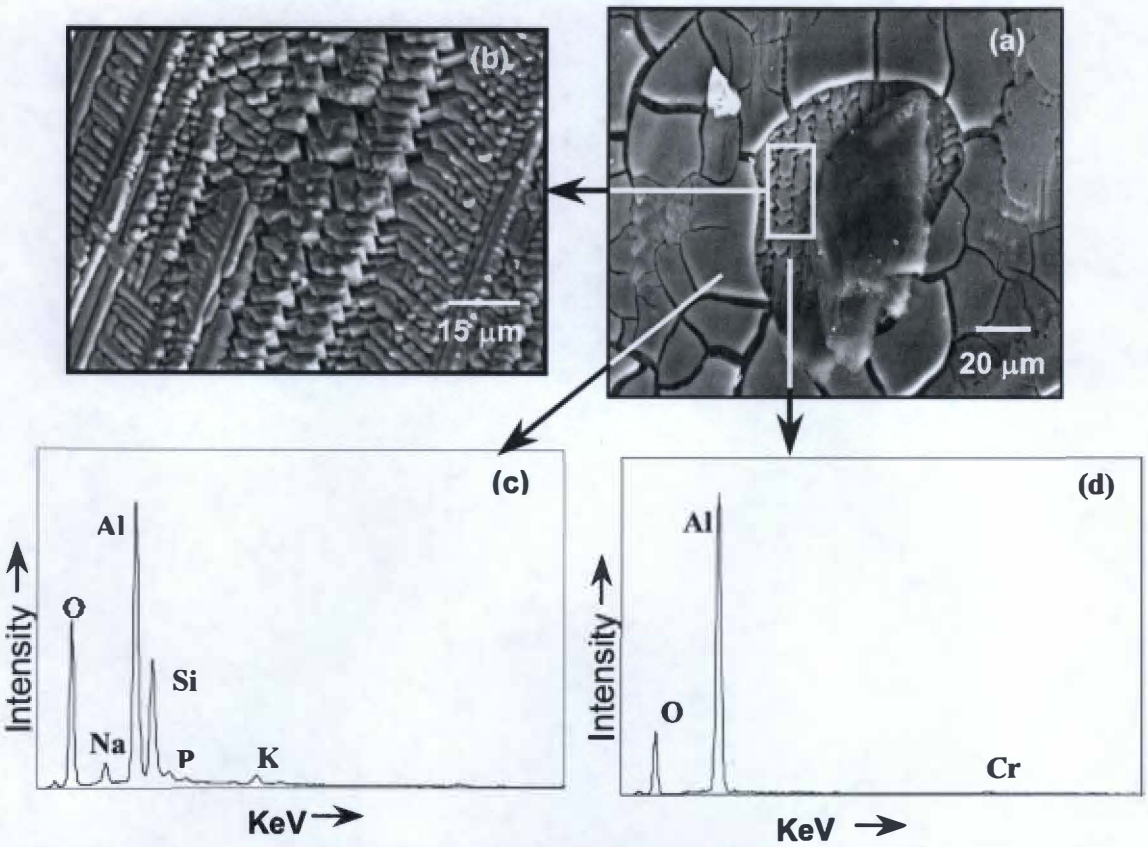

FIGURE 2.9: Microstructural analysis of the resolidified layer near the ridges (a) glassy surface layer and refined subsurface layer, (b) refined subsurface layer in magnified view, (c) EDS spectrum of the refined layer and, (d) EDS spectrum of the glassy layer.

Similar partial vitrification of alumina/silica-based compound has also been reported earlier [19]. The presence of a glass layer can make the surface brittle and hence formation of such a glass phase needs to be avoided by proper adjustments in the wheel and bond material composition and also the processing conditions.

The morphological modifications on the surface of the wheel are a result of the rapid solidification taking place during the process. The thermal conditions present during laser-dressing control the nature of solidification structure formed. Thus, the calculation of cooling rates, thermal gradients, etc. during laser-dressing is very important in order to understand and control the process.

3. THERMAL EFFECTS

Surface processing of ceramics by laser offers potential advantages such as, precise control over high input of thermal energy at spatial levels, rapid processing speed and unique modification of microstructure due to rapid heating, remelting, solidification and cooling. The depth of laser energy penetration into the wheel surface is constrained by the laser travel speed and the power input. Increasing irradiation time will allow the laser energy to penetrate deeper into the material and cause more melting. Laser-dressing of Al_2O_3 grinding wheels show modification in the morphological features on the surface [Section 2.3]. Depending upon the laser processing parameters used, melting (followed by resolidification) and/or vaporization resulted in change of surface topography (morphology and composition) and microstructure.

The microstructure formed on the surface of the laser dressed wheel depends on the temperature gradient and cooling rate. These in turn depends on the heat input that is a function of the laser power used for processing. Alumina being a ceramic material has a poor thermal conductivity (Table 2.2) as compared to metals; therefore it tends to retain the heat for a longer time. Furthermore, presence of original porosity in the alumina wheel reduces the thermal conductivity [20], resulting in heat dissipation at a much slower rate. Laser-dressing results in a decrease in the amount of porosity in the resolidified layer on ceramic materials due to consolidation of the surface structure. Thus, estimation of the cooling rate is important to have an understanding of the evolution of

microstructure and texture on the surface during laser processing. There are many models for predicting the formation of various microstructures during several different rapid solidification processes [21,22,23].

This chapter deals with experimental determination of cooling rates to study its effect on the solidification structure during laser-dressing. An attempt is made to correlate the microstructure formed on the wheel surface after laser-dressing to the cooling rates in order to understand the multi-faceted nature of grains. A two-colored pyrometer is used for the experimental calculations of the cooling rates during the process.

3.1 Pyrometric Temperature Measurement

Commercially available two-color optical pyrometer (Chino model IR-FBQ1H) equipment was configured for the measurement of temperature during laser-dressing of the alumina grinding wheels. The temperature range covered by this instrument is 600-1500 °C and its response time is 0.5 ms. An optical pyrometer based on the measurement of the intensity of light over a single wavelength region is very difficult to calibrate and to maintain in calibration. Drift in optical detector sensitivity is always present, sometimes unpredictable, and correction methods for it are often difficult to implement. Multi-color pyrometers, especially two-color have come into favor because many of the errors inherent in the single detector pyrometer are cancelled when the ratio of the signals from two detectors is taken. Additional advantage of using a two-color pyrometer is that,

the apparatus is remote and protected from the high temperature region, and that the measurement is non-intrusive.

3.1.1 Principle of Two-Color Pyrometer

Light emanating from an incandescent processing area is collected by small telescope and passed by an optical fiber to the two-color pyrometer. A 50/50 beam splitter passes half of the collected light through an optical filter having a center wavelength of λ_1 microns while passing the other half through a second filter whose center wavelength is λ_2 microns. Two detectors, one each for the filtered light beams at wavelengths 1.35 and 1.55 microns (in case of the Chino pyrometer) generate signals whose ratio is a function of the temperature of the incandescent surface.

3.1.2 Calibration of Pyrometer

The commercially available pyrometers have an internal circuitry to compute the ratio of the detector signals and also to linearize the signal ratio versus temperature. The output of a Chino instrument, for example, is a single signal providing 1 mV/°C, but the ratio, linearization, and scaling circuitry limits the temperature range that can be covered. The raw signals from the two detectors can be used to extend the temperature range over which the pyrometer operates. Hence, the pyrometer was calibrated to measure temperatures upto 2000°C. A commercial temperature transfer standard in the form of a rather slow response but highly accurate two-color pyrometer (Mikron Model M190V-TS, SN 033641, calibration certificate no. 7138) was used for calibration. This transfer

standard is annually returned to its manufacturer for calibration against NIST traceable temperature standards, and has an absolute accuracy of 10°C over the range 800-3000°C. The only operational attribute of this instrument preventing its direct use for temperature measurement in materials processing is its slow response.

3.1.3 Collection Optics

The collection of too much light from the incandescent region causes detector saturation, too little collected light results in noisy signals, and the stray light whose wavelengths fall within the bandpass of either spectral channel of the pyrometer cause spurious temperature readings. Signal strength is also influenced by the size of the 'detector sensitive area image' that is focused on the workpiece. A special telescope was used to collect the light signal from the sample surface during processing (Figure 3.1). Light enters from the left. The aperture on the conical baffle rejects light not emanating from the focal spot of the collimating lens. The optical filters on the Chino collection optics lacked adequate rejection of the very strong stray light from the laser at 1.064 microns (Nd:YAG laser wavelength). Therefore, a wavelength rejection filter with a rejection ratio of $1:10^6$ was added. This laser line rejection filter sits between the collimating and focusing lenses, and the latter brings the collected light to focus on the end of the optical fiber. The other end of the fiber attaches to the pyrometer. It is important to note that the telescope, fiber, and pyrometer are calibrated as a single unit.

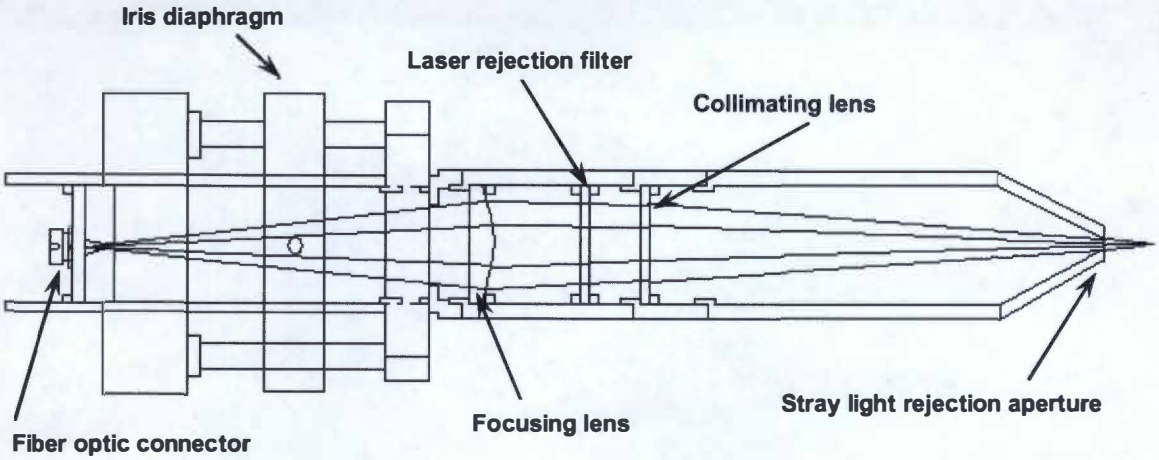

FIGURE 3.1: Telescope (collection optics) used with the pyrometer to collect the light intensity signal from the source.

3.1.4 Instrumentation

A schematic of the experimental setup for the temperature measurement during laser-dressing of the ceramic alumina grinding wheels is shown in Figure 3.2, and Figure 3.3 shows the complete instrumentation for the temperature measurement setup in terms of a block diagram. The telescope (collection optics) of the pyrometer was mounted on the motion system and is focused at the same spot where the laser beam is focused. As many as three pyrometers can be operated simultaneously with minimal interference with the materials processing. The collected signal is transferred to a data acquisition system via a fiber optic cable. A 16-bit analog-to-digital data acquisition system (Data Translation model DT 9804) was used to record pyrometer signals. The precisely controlled motions

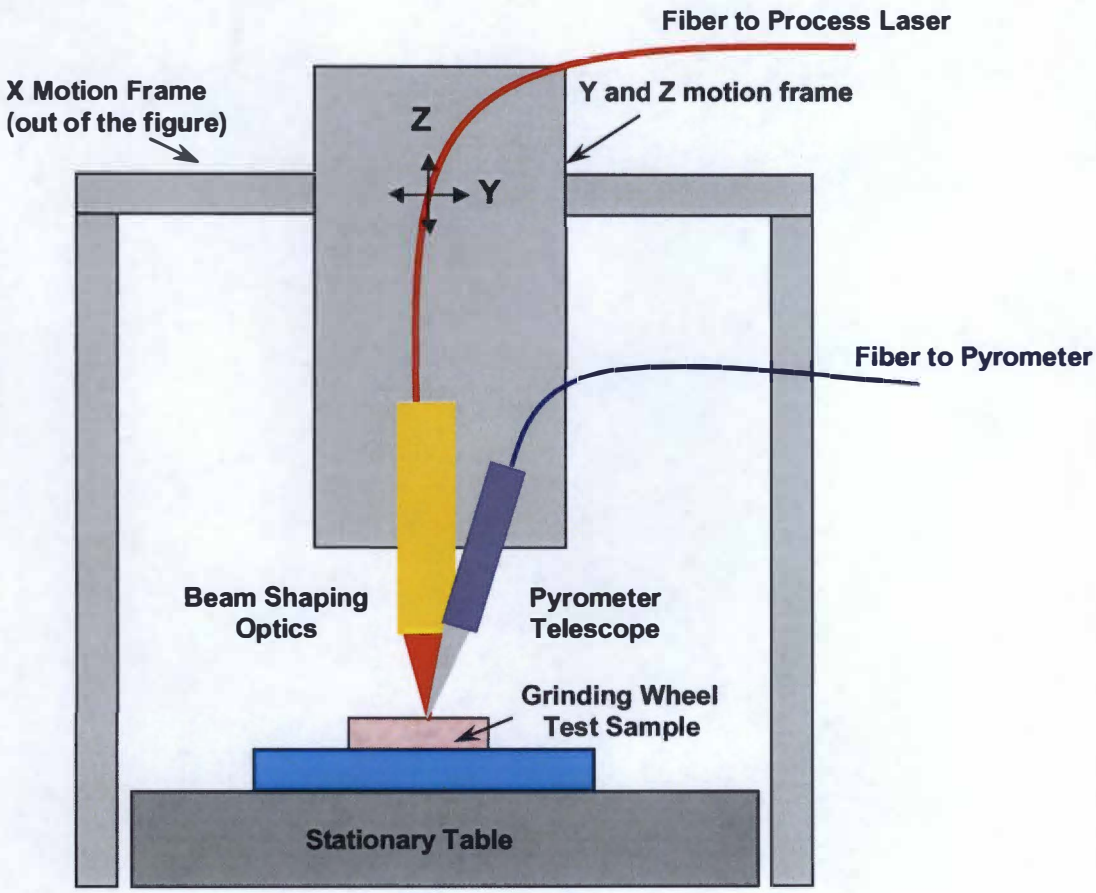

FIGURE 3.2: Schematic of the experimental setup for temperature measurement.

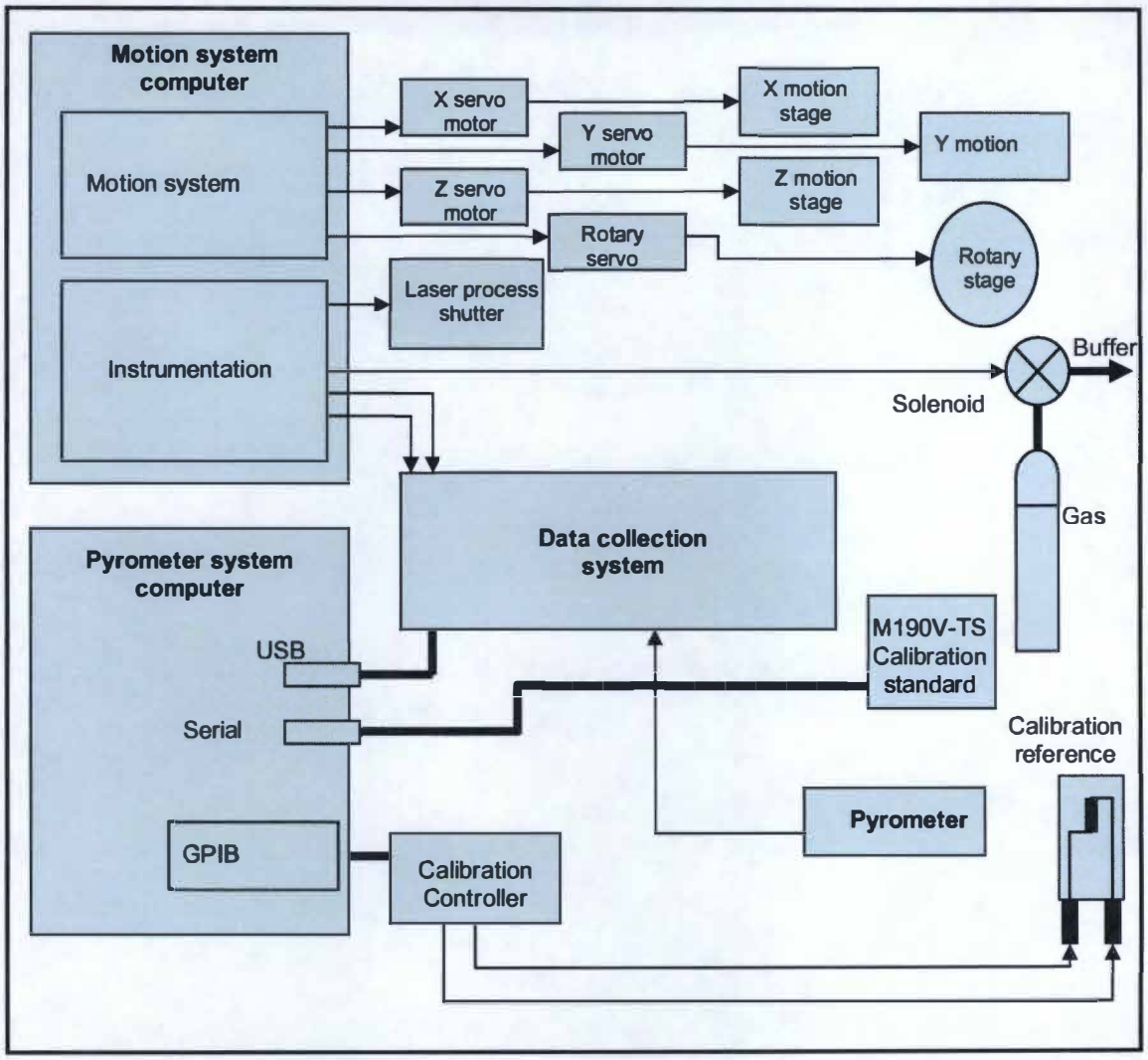

FIGURE 3.3: Instrumentation for the optical Pyrometric temperature measurement experiment.

inherent in laser processing impose the requirement that data acquisition equipment configured to observe and record the processing, be synchronized with the motion system. A visual basic computer program especially written to control the pyrometer operation, data collection and processing was used. The program receives "motion start" and a "laser shutter open" signals from the motion system and records temperature whenever the laser shutter is open as long as motion continues. Temperature vs. time plots, are directly plotted during the laser-dressing process, from which the cooling rates are estimated.

3.1.5 Integration of Pyrometer with the Laser Motion System

Laser materials processing require precisely controlled motion system. This makes mounting of the pyrometer on the motion system essential, to be able to detect and record the instantaneous signal (temperature data) from the spot where the laser beam was focused on the sample. A flexible optical fiber was used between the collection optics, called telescope here, and the remaining pyrometer components, in order to locate pyrometer electronic components and as many optical components as possible, away from the heat and fumes from the processing region. Safety and processing requirements also determine when the laser shutter will be opened and closed. The computer program written especially for processing the data obtained from the data collection unit was modified for the pyrometer to be synchronized completely with the laser motion system without any outside interference as described earlier.

When processing ceramics at higher laser powers, a big plume (Figure 2.2) is observed on the sample surface which interferes with the signal intensity of light collected. This plume emits a white light and hence use of a single filter in the collection optics, to reject it is not possible. The plume causes saturation in the collected signal giving erroneous results. Thus to overcome the problem due to plume, and to measure instantaneous temperature data directly at the spot where laser had been positioned, a delay of 5 seconds was given for the fly back of the laser, before processing the next track. During this time the laser stays at the end of the processed track and the laser shutter remains off, but the pyrometer keeps recording temperature data continuously at that spot as the sample cools. Thus, as the plume effect gradually disappears after the laser beam is turned off, the pyrometer starts recording real time temperature data. However, for the high powers (1000 W in the present case), volume of the plume is very large and it exists for a longer time (>3 sec) over the sample surface after the laser beam has been turned off, thus saturating the pyrometer detector signal. During this time the temperature of the sample dropped substantially (to ~ 400 °C). For such a low temperature, the filtered pyrometer detector has very low sensitivity to record accurate temperature values. We observed almost a burning flame on the sample during laser processing at 1000 W. Thus, temperature data was recorded for the 400 and 500 W samples only. At these power levels, the plume was small and short lived (< 1 sec) to not to saturate the pyrometer detector signal for recording the accurate temperature data.

3.2 Estimation of Thermal Conditions

Rapid solidification tends to show advantages such as refined microstructure and reduced microsegregation. In laser processing of materials, very high cooling rates are observed over a small region of workpiece where non-equilibrium microstructures are produced due to rapid solidification. A high heat input from the laser beam to melt in a localized area on the sample surface, can achieve high cooling rates and the cooling rate will be different from center to edge of track causing a change in microstructure. Laser irradiation can be approximated as a point energy source on the surface, with heat flowing in all directions into the material being processed. The system can be assumed to attain a quasi-steady state when the travel velocity of the melt/solid interface becomes constant [24]. Incident radiation is partly reflected and partly absorbed by the material. Some amount of adsorbed energy is lost by re-radiation and convection, while rest is conducted into the substrate. Heat energy is supplied by the laser at the top surface of track, which sets up convective currents inside the melt pool and provides fast dissipation of heat at the melt/solid interface.

The experimentally determined cooling rates during laser processing at two different powers (400 and 500 W) are given in Table 3.1. These are calculated from the temperature vs. time data, as shown in Figure 3.4, obtained directly from the experiments using the pyrometer. Curve fitting of the plots gives the time dependent equation for the temperature, the slope of which is the cooling rate. The fitted curve is extrapolated to the melting temperature of alumina to estimate the cooling rate near the melting point. It is

TABLE 3.1: Cooling rate results.

Laser Power (Watts)	Cooling Rates $\left(\frac{dT}{dt}\right)$ (°C.s^{-1})			
	Track 1		Track 2	
	Max dT/dt at melting temperature	dT/dt at a time, t = 2.2 sec, after start of solidification	Max dT/dt at melting temperature	dT/dt at a time, t = 2.2 sec, after start of solidification
400	- 770.8	- 437	- 702.8	- 382.8
500	- 701.5	- 401	- 580.6	- 299.7

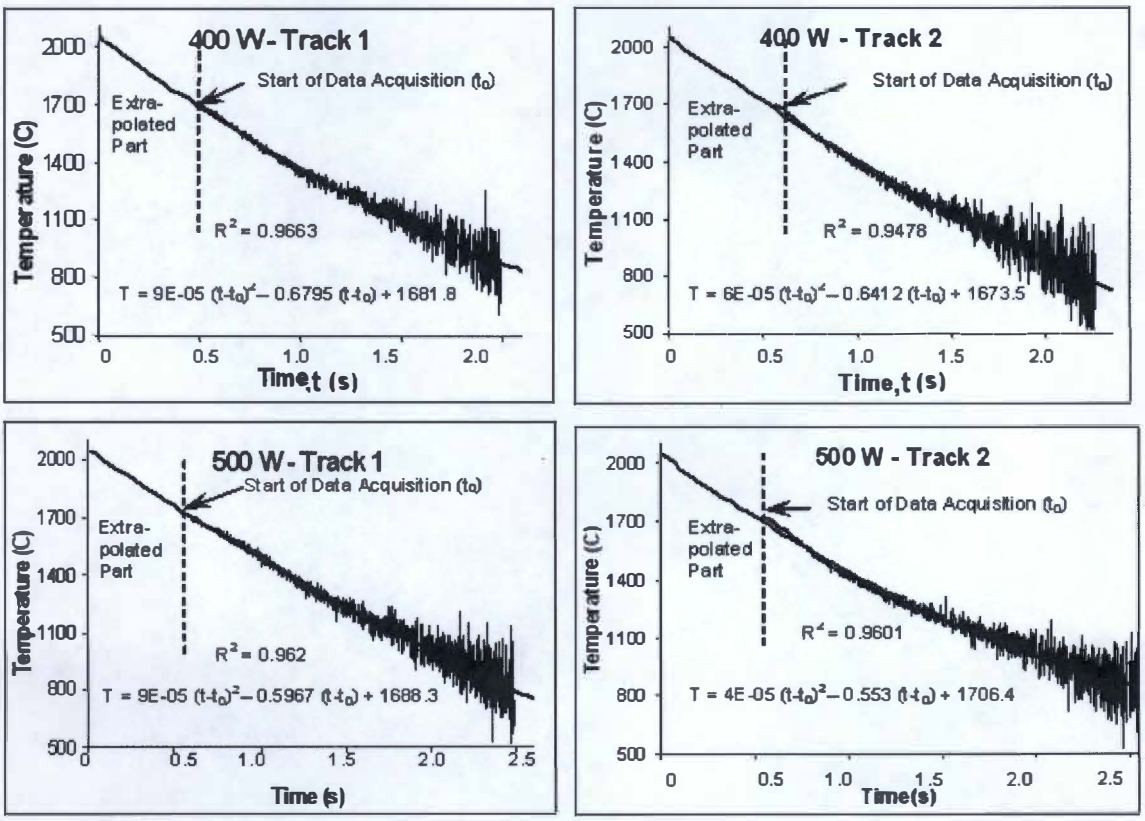

FIGURE 3.4: Temperature vs. Time plots obtained experimentally, for two tracks on the 400 W and 500 W laser-dressed samples.

assumed that the time vs. temperature relation remains reasonably the same, as obtained in the range of temperature data acquisition. The actual data acquisition starts at time t_0 as indicated in the plots. This is due to the fact that the pyrometer requires some time to come out of saturation (after the laser beam is switched off) and start recording data. For the temperature vs. time plots in Figure 3.4, the scatter in the measured temperature data near the lower temperature range of the pyrometer is higher than the upper temperature range, due to an increase in the signal-to-noise ratio. This is due to a relatively low intensity of signal collected from the sample surface at lower temperatures compared to at higher temperatures. The cooling rate equations are time dependent, thus using these cooling rates can be calculated at any time after the solidification starts. Data is given for two adjacent tracks and cooling rates calculated at the melting temperature (2050°C) of alumina, which can be assumed to be the maximum cooling rate during the process, and also at a time 2.2 sec, corresponding the lower calibrated temperature range (~ 850°C) of the pyrometer. The cooling rates obtained in sample processed at higher laser power are lower as compared to that of the ones at lower power. This can be explained from the fact that; being a poor conductor of heat, alumina tends to retain heat for a longer time as compared to metals. When other parameters such as alumina sample porosity, experimental environment, etc. remain same and the only factor changing is the laser beam power, an increase in heat input to the sample (i.e. increase of laser processing power) causes a greater heat build up, a larger melt zone and an increase in the interaction volume. Thus, it takes more time to dissipate this heat causing a drop in the cooling rates. Hence for further higher laser powers (like 1000 W), the cooling rate can

be expected to be slightly lower as compared to that calculated for the lower powers (500 and 400 W).

Another notable observation is that the cooling rate in the second track is slightly lower than that in the first track for both the 400 and the 500 W samples. As the laser passes over the first track, it preheats the adjacent material, resulting in a decrease in the thermal gradient, which in turn directly decreases the cooling rate for the second track. Table 3.1 gives the cooling rate at the time of 2.2 second after solidification starts. This is the time when the corresponding temperature of the sample is near the lower calibrated temperature range of the pyrometer used for experimental temperature measurements. The trend observed in the cooling rate at this time is similar to that seen at the solidification temperature, but the cooling rates are much lower due to lower thermal gradients and heat loss from the sample. Solidification occurs in a direction opposite to that of heat extraction. As an assumption is made that the laser acts as a point source for energy input on the surface of sample and heat is extracted in all directions into the material being processed, it is expected that grain growth on solidification and the microstructure formed will be in accordance to this heat extraction model. The microstructure evolution during laser-dressing of alumina with various combinations of processing parameters that result in varying thermal conditions is discussed below.

A range of microstructures (such as planar, cellular and dendritic) which are observed in laser processed materials are due to the different solidification conditions present [25, 26]. A

planar solidification front is observed when the interface is exactly at the equilibrium liquidus temperature and when every point in front of the interface is above the liquidus temperature. Thus any instability formed on the interface dissolves back into the liquid. If melt is supercooled in front of the interface then any instability or perturbation formed on the interface will grow fast into the supercooled liquid. Under a positive temperature gradient, constitutional supercooling is solute driven. The ratio of G/R, where G is the thermal gradient and R is the solidification rate, governs the type of solidification structure formed during constitutional supercooling [25, 26]. Increasing the G/R ratio causes a progressive change in the solidification characteristics, from fully dendritic to cellular-dendritic, to cellular and finally to planar. Thus, the calculation of the G/R ratio during laser-dressing can help explain the microstructure formed within the laser track based on the thermal conditions present.

When the Al_2O_3 ceramic grinding wheels are subjected to laser energy, the sample surface melts and resolidifies changing the surface morphology. The solidification structure in a single track varies with distance from the center of the track (which is along the Y-direction in Figure 3.5). As shown in Figure 3.6, at the center of the track, particles are multifaceted and equiaxed having a dendritic structure on them; whereas at the edges or the region of overlap between two adjacent tracks, the grains are elongated in shape (columnar) with growth taking place in a direction (Y-direction) cooling rates. Such strong dependence of type and pattern of grain structure evolution can be further understood from heat transfer behavior during dressing, as explained below.

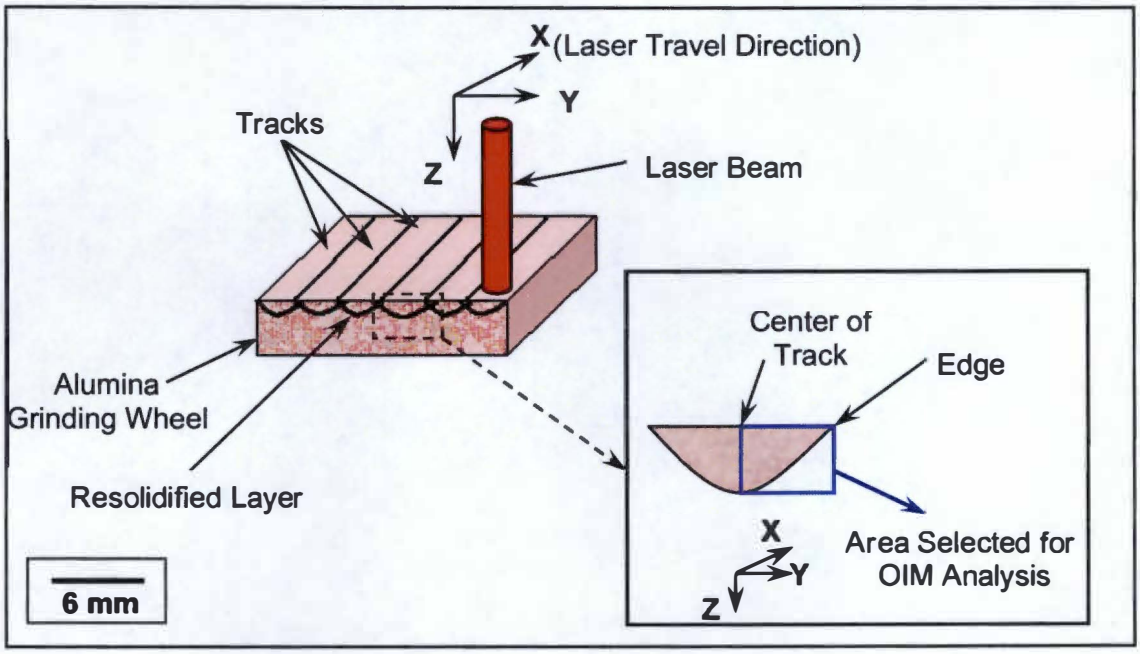

FIGURE 3.5: Co-ordinates of the alumina sample during laser-dressing. The inset has one of the laser-dressed track (width ~ 3 mm) in cross-section showing the area selected for the OIM analysis.

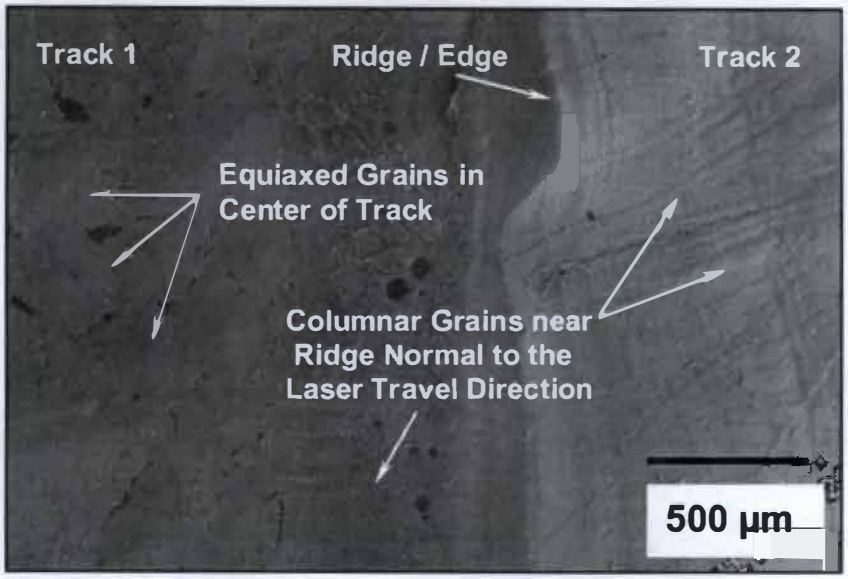

FIGURE 3.6: SEM image showing columnar growth near the edges and equiaxed grains with dendritic structure in the center of the track.

The general equation of heat transfer for a moving heat source, is given by the Equation 3.1 in which the 'substantial derivative' of temperature [a function of position and time, i.e., T = T (y, t)] is given by the partial derivatives [27, 28, 29, 30].

$$\frac{d}{dt}[T(y,t)] = \frac{\partial T}{\partial t} + \frac{\partial y}{\partial t} \times \frac{\partial T}{\partial y} = D\frac{\partial^2 T}{\partial y^2} + \frac{\dot{q}}{C_p \rho} \qquad [3.1]$$

For the time independent situation, i.e., quasi-steady state heat transfer for moving origin problem, the time-derivative of temperature tends to zero in Equation 3.1. Hence, the surface-cooling rate $\frac{dT}{dt}$ in the direction opposite to laser traverse under quasi-steady state ($\frac{\partial T}{\partial t} = 0$) can be estimated as per the relation :

$$\frac{dT}{dt} = \frac{dT}{dy} \times \frac{dy}{dt} \quad or \quad G = \frac{1}{v} \times \frac{dT}{dt} \qquad [3.2]$$

where, v is the laser beam travel velocity. Thus the thermal gradients *(G)* are calculated from the temperature vs. time plots assuming quasi-steady state using Equation 3.2.

During solidification, the velocity of the liquid/solid interface or the growth rate *(R)* is given by the Neumann solutions to the Stefan Problem [31]. Assumptions are made that there exists strong convective currents in the melt pool and that the total energy absorbed at the free surface of the liquid is instantaneously transported to the interface by convection. The solution to Stefan problem is:

$$V_i \rho \Delta H_m - \kappa_s \frac{\partial T}{\partial y} = V_i \rho [\Delta H_m + C_p (T_m - T_o)] = I_a \qquad [3.3]$$

where, V_i is the liquid/solid interface velocity. Equation 3.3 gives the average velocity of the interface during the time that the treated zone solidifies. The solidification front velocity (in the initial phase, i.e. at the start of solidification) is greater than what Equation 3.3 estimates. At the start of solidification, the local temperature gradient is very large and this leads to maximum interface solidification velocity, which is approximated by

$$V_i^{\max} \approx \varsigma \left(\frac{D}{\tau_1} \right)^{1/2} \qquad [3.4]$$

where, τ_1 is the laser beam dwell time and ς is given by the solution of

$$\varsigma\,[1 + erf(\varsigma)]\exp(\varsigma^2) = \frac{c_p(T_m - T_o)}{\pi^{1/2}\,\Delta H_m} \qquad [3.5]$$

It is seen from the above equations that the average and the maximum interface solidification rates are highly dependent on the laser beam intensity and traverse speed.

Using Equations 3.3 and 3.4 respectively, the travel velocity (V_i) of solid/liquid interface i.e. the growth rate (R) is calculated at the center of the track, and at the edge where a maximum growth rate is observed, as the solidification front approaches the center of the track from the edge. Using the G and R values thus obtained, the G/R ratios are calculated and given in Table 3.2. The ratios are very high near the edge of the track where the solidification starts and decrease towards the center. As Equation 3.4 is used for calculating the growth rate (R) near the edge i.e. at the start of solidification, the G/R ratios for the edge are of the same magnitude for all the processing powers. As mentioned earlier, it is interesting to note that the solidification structure observed within a laser track varies from equiaxed grains with dendritic structure at the center of the track, to columnar grains near the edge (Figure 3.6). Also as stated earlier, the constitutional supercooling theory predicts that, increasing the G/R ratio causes a progressive change in the solidification characteristics, from fully dendritic to cellular-dendritic, to cellular and finally to planar. Similar trends in the calculate G/R ratios is observed within a laser

track. These definite regional patterns in grain structure in turn may have influence on the crystallographic structure. Evolution of specific crystallographic orientations may have strong bearing on microscopic level morphological features and, therefore, grinding/machining characteristics of laser-dressed sample. Attempts are made to study crystallographic texture and their influence on grinding/machining performance.

TABLE 3.2: G/R ratios for various processing parameters.

Part of Track	G/R ratios for Laser Power:			
	400 W		500 W	
	Track 1	Track 2	Track 1	Track 2
Center	4.43×10^6	4.04×10^6	4.03×10^6	3.34×10^6
Edge	1.735×10^9	1.735×10^9	1.735×10^9	1.735×10^9

4. EVOLUTION OF CRYSTALLOGRAPHIC TEXTURE

Identification of planar textures due to laser-dressing is important as the (atomic) planar density is expected to influence the formation of the types of crystallographic planes that in turn will have strong bearing on the grinding characteristics. Growth along preferred planes can play important role in the morphological modification on the surface of the grinding wheel after laser-dressing which results in the formation of grains with cutting edges and vertices. X-ray diffraction (XRD) and pole figure analysis are useful tools to analyze the possible texture on the sample after laser-dressing.

4.1 Bulk Surface Texture

A Philips Norelco X-Ray diffractometer with CuK_α radiation operated at 40 kV and 15 mA was used to characterize the dressed wheel surface in terms of the phases present. Furthermore, pole figure measurements were performed for possible texture, using a Philips X'Pert Analytical Diffractometer. The operating conditions were maintained at 45 kV and 40 mA, using CuK_α radiation through a point source. Reflection method was employed for pole figure analysis with ϕ varying between 0° to 360° and ψ between 0 to 85°. Planes with higher relative intensity in the normal XRD (2θ versus Intensity) plots were analyzed for their pole figures.

X-Ray diffraction analysis of the undressed as well as the laser-dressed alumina samples, revealed corundum (α-Al_2O_3) as a primary phase present (Figure 4.1). The intensities, however of few individual peaks were significantly higher than that of others in the laser-dressed samples, indicating preferential orientation along some crystallographic planes. The peak corresponding to (116) plane was most prominent in the undressed sample (Figure 4.2a), whereas the relative integrated intensity of this peak reduced substantially in the laser-dressed material. Furthermore, (110) plane, which was almost in the background in the undressed sample, became the plane with the highest intensity after laser-dressing (Figure 4.2b). These changes clearly indicated the growth along preferential crystallographic changes on the alumina grains. Non-equilibrium condition during laser treatment is likely to provide multiple preferential orientations.

Further detailed evaluation of possible crystallographic texture due to additional planes was conducted using pole figure analysis. Table 4.1 summarizes these additional poles and the corresponding planes. Also, it qualitatively compares the nature of pole figures obtained for these poles at different laser powers as well as in the undressed grinding wheel. Scattered peaks in the pole figure indicate absence of any preferential orientation, whereas if the peaks are concentrated symmetrically about the center, then the sample has a preferential orientation for that plane. In general, the planes (012), (104), (110) were scattered in the undressed sample, whereas after laser-dressing, they were concentrated about the center. The x-ray diffraction results for the (116) plane were confirmed by the pole figure analysis, where the poles are concentrated around the center for the undressed

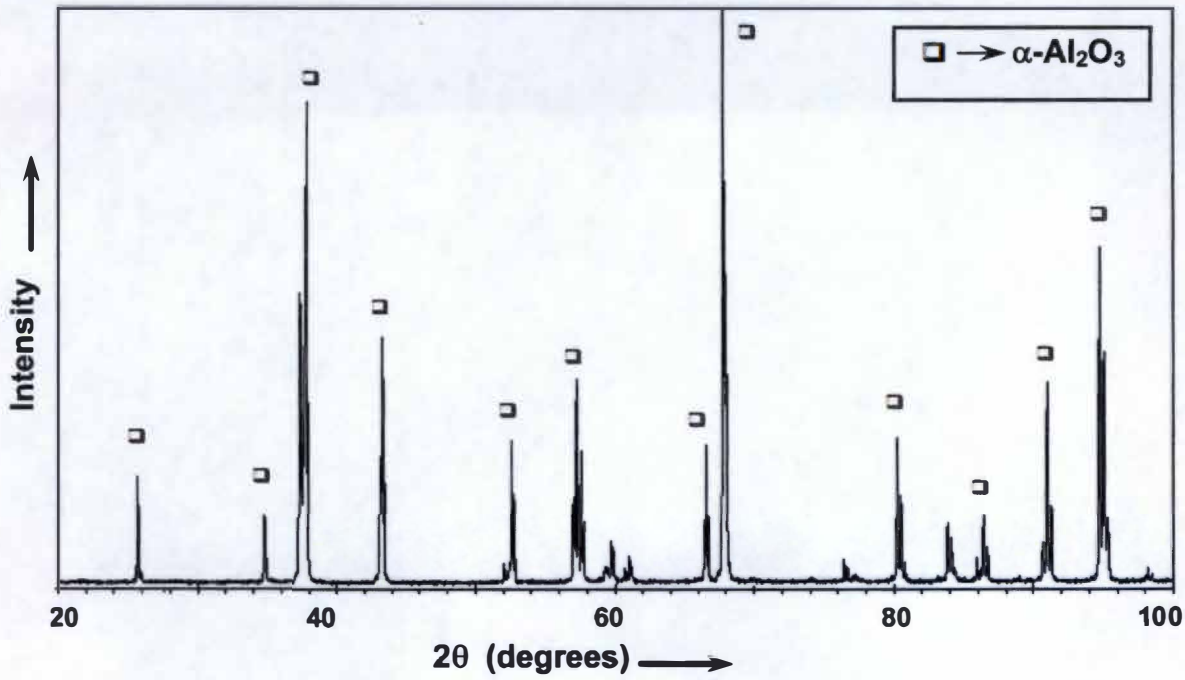

FIGURE 4.1: XRD spectra of a 1000 W laser-dressed sample showing α-Al_2O_3 as the phase present.

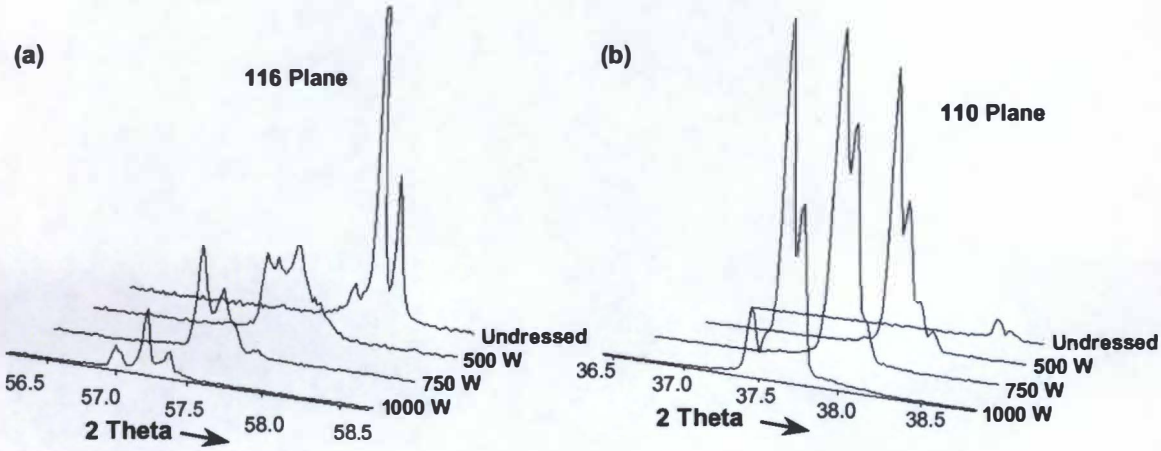

FIGURE 4.2: XRD spectra as a function of laser power for (a) (116) plane and (b) (110) plane.

TABLE 4.1: Qualitative comparison for the pole figure analysis at different 2θ angles for the undressed and laser-dressed samples at different powers.

$2\theta^0$	Plane	Undressed Sample	Laser-dressed Sample		
			500 (W)	750 (W)	1000 (W)
25.57	(012)	S	CC	CC	CC
57.50	(116)	CC	S	S	S
37.76	(110)	S	CC	CC	CC
66.50	(214)	S	R	R	R
35.15	(104)	S	CC	CC	CC

Legend:
S- Scattered.
CC- Concentrated about the center in a symmetric way.
R- Poles are arranged in a concentric ring about the center.

sample (Figure 4.3a) and scattered for laser-dressed wheel (Figure 4.3b). The labels on the pole figures indicate the intensity of the line profiles of the peaks. The pole figure analysis of the (110) plane is shown in Figure 4.4. In the (110) pole figure for the undressed samples, the poles are more scattered and are away from center (Figure 4.4a), where as for the laser-dressed sample, poles are concentrated around center in a symmetric way (Figure 4.4b), where as for the undressed sample. Thus for the laser-dressed sample, the (110) plane has a preferential orientation. For the (214) plane, the poles were scattered in the undressed condition (Figure 4.5a), but after dressing most of them were arranged in a concentric rings about the center (Figure 4.5b), indicating orientation of the peaks at an angle to the sample surface. The faceted structure on the surface of particles is possibly a result of such preferred orientation. Figure 4.6 shows such multifaceted particles with cutting edges and vertices, on the surface of the laser-dressed grinding wheel.

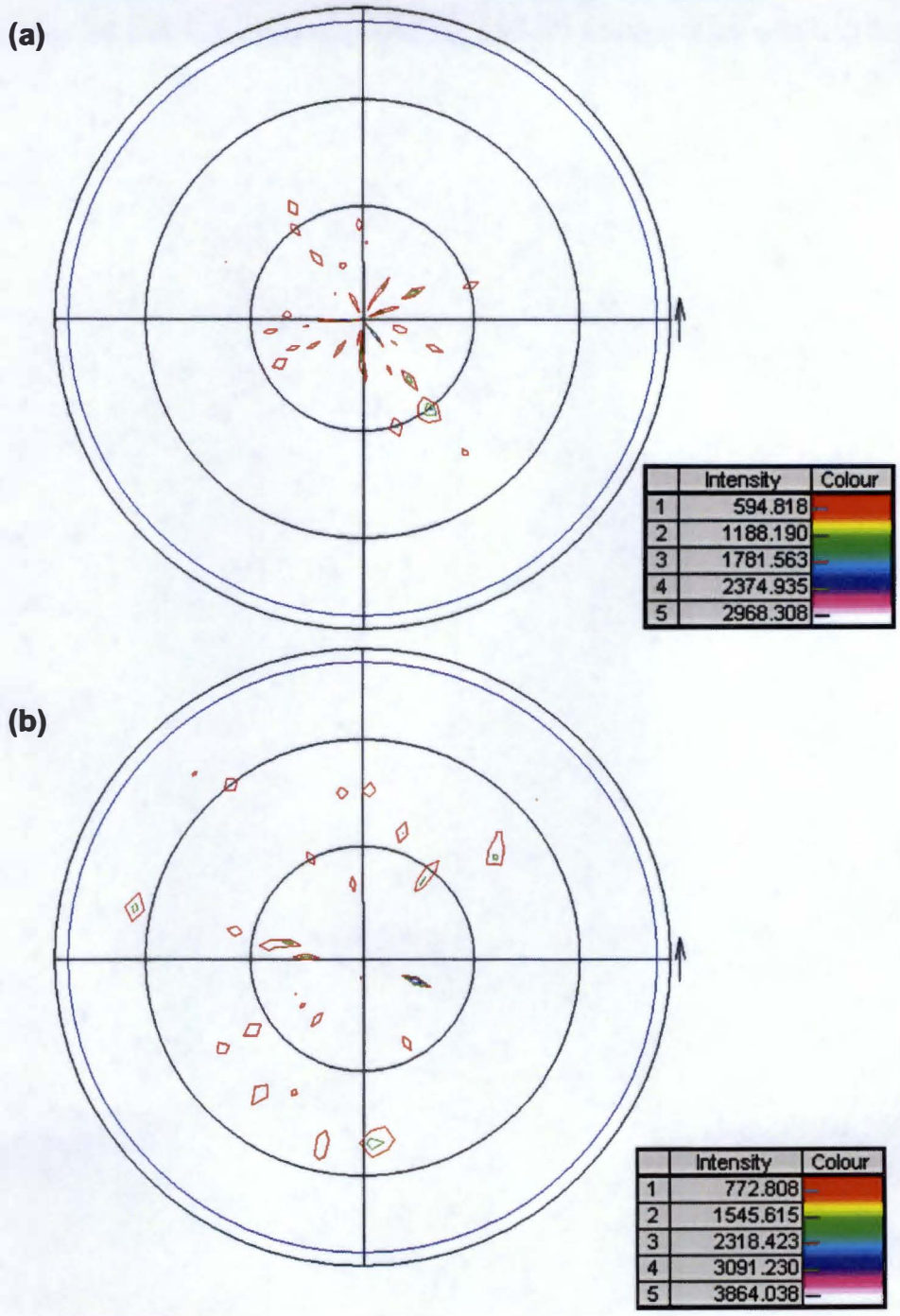

FIGURE 4.3: Pole figure for (116) plane in (a) undressed sample and (b) laser-dressed sample.

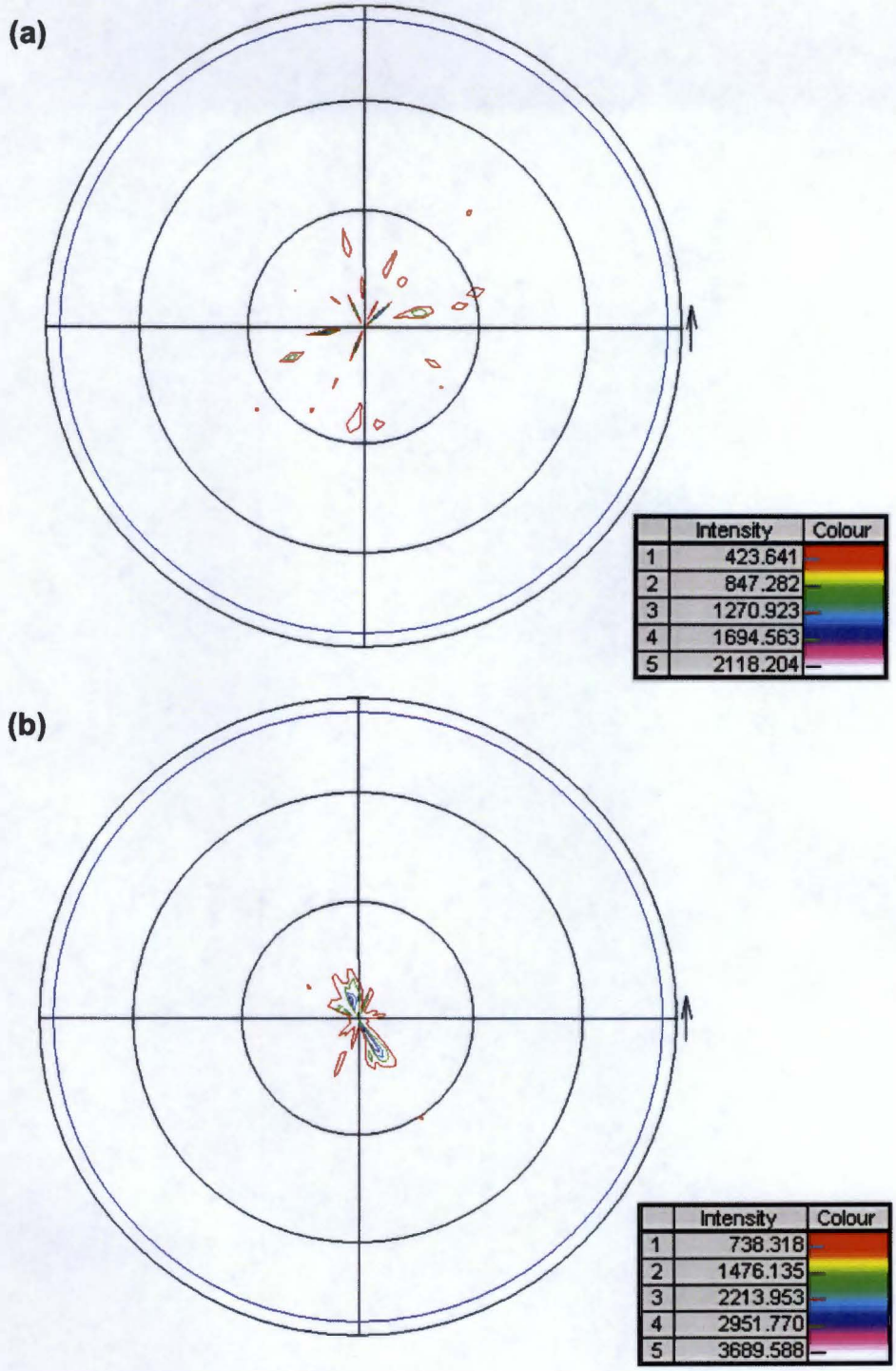

FIGURE 4.4: Pole figure for (110) plane in (a) undressed sample and (b) laser-dressed sample.

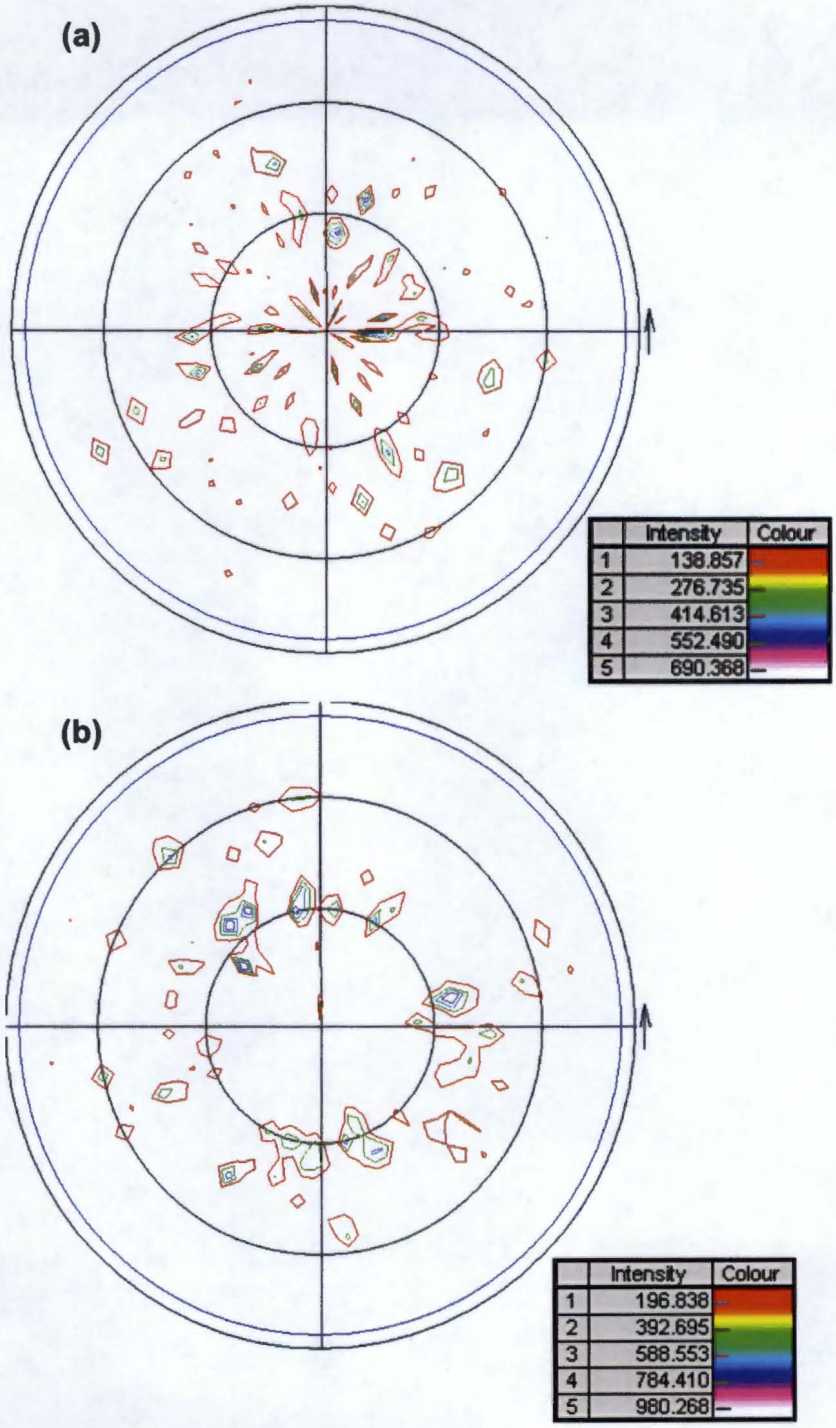

FIGURE 4.5: Pole figure for (214) plane in (a) undressed sample and (b) laser-dressed sample.

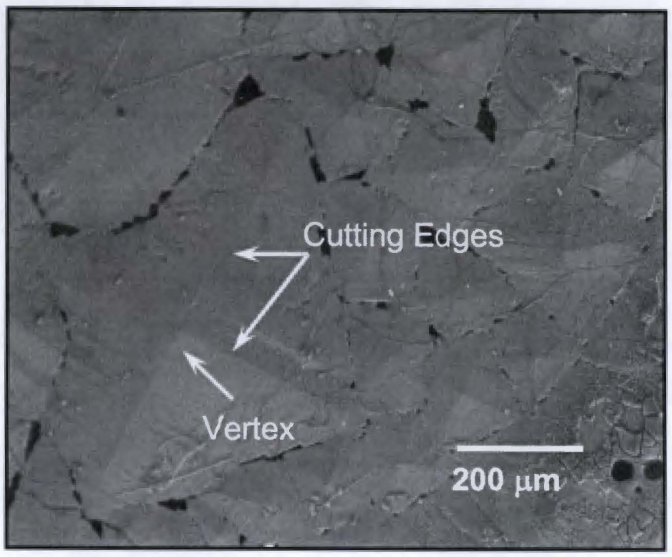

FIGURE 4.6: Morphological features on a laser-dressed sample (750 W).

These XRD-based evaluations for crystallographic texture are from the top surface of laser-processed sample. However, due to penetration of laser energy (heat transfer) into the finite depth of sample volume, crystallographic changes are also expected within the subsurface heat affected zone (inset in Figure 3.5). These crystallographic changes in subsurface region due to its small volume is probed using orientation imaging microscopy (OIM) technique as discussed in the following section.

4.2 Grain/Subgrain Structure

The x-ray diffraction (XRD) experiments indicated formation of crystallographic texture on the surface of dressed wheels. Pole figure analysis [Section 4.1], indicated preferential orientation along the (110) plane. The mechanical properties of directionally solidified

structures, such as the ones produced after laser-dressing, are very sensitive to microstructure and crystallographic texture, which can vary with processing conditions. It is necessary to qualify fully the microscopic and crystallographic texture in order to predict the material performance. Pole figure analysis by x-ray diffraction is a standard and useful technique for measuring crystallographic texture, and provides information averaged over the diffraction volume. In order to evaluate the effect of texture produced in the laser-dressed alumina grinding wheel, on the overall grinding process, microtexture information is needed. Orientation Imaging Microscopy (OIM) [32] is used for this purpose in the present study. OIM gives phase specific crystallographic information.

In conventional optical microscopy technique, it is difficult to distinguish between small and large misorientation differences amongst the grains as it gives contrast due to chemical etching of the grain boundaries. Though transmission electron microscopy (TEM) reveals all changes in the orientation, the area from which the information is obtained is very small and the overall orientation information for the sample is missing. XRD provides average texture data from a large area, but it neither provides any information on the spatial distribution nor the interrelation of individual grains and sub-grains. In OIM, the local orientations are obtained from Kikuchi patterns, in a manner similar for TEM, but are produced from the surface of a bulk sample. Hence the patterns can be obtained from much larger area on the sample surface, giving more global information regarding the microtexture present in the test sample. Hence to study the local orientation in the laser-dressed grinding process, OIM was employed.

To generate good quality Kikuchi patterns from Al_2O_3 ceramics, polishing is unavoidable. The backscattered electrons used to obtain Kikuchi patterns are generated at a typical depth of 50-200 nm; hence any imperfections close to the sample surface will deteriorate the quality of patterns. For polishing the Al_2O_3 ceramic samples, they were first mounted in cross-section to expose the resolidified top layer of the laser-dressed samples, and then wet polished using standard SiC grinding papers (600, 800, 1200 mesh). This was followed by polishing using colloidal silica paste (2 μm grain size) and then a diamond paste (1 μm grain size) with water as a lubricant. A very slow rotation speed (30 rpm) of the polishing disk was used without exerting too much pressure to avoid surface damage (Polishing machine: Buehler Phoenix-Beta with automatic specimen motion). Since the Al_2O_3 ceramic samples are non-conductive, the specimens were first carbon-coated. The thin coating and the low atomic number of carbon minimized the absorption of the backscattered electrons. Copper tape was used to ground the sample to the holder and SEM.

Electron backscattered diffraction (EBSD) patterns which are also called backscattered Kikuchi patterns, were generated at 20 kV in a commercial Philips XL30 FEG SEM equipped with a TSL orientation imaging microscopy (OIM) system [33, 34, 35] using a special CCD camera. OIM was done at the Oak Ridge National Laboratory, TN, USA under the SHaRE User Program. In order to obtain EBSD patterns, the sample was steeply tilted to about 70° from horizontal, i.e. 20° with respect to the incident electron

beam in the SEM. The quality of the EBSD Kikuchi pattern is a function of this angle, the electron beam voltage, and the sample surface quality.

The electrons that produce the EBSD pattern are a small fraction of the total scattered electron signal. In order to subtract this background signal, a background image was obtained with the electron probe scanning and that image was subtracted from each acquired EBSD pattern prior to indexing. To produce crystallographic orientation map, the electron beam is scanned over a selected surface area and the resulting EBSD patterns are automatically indexed and the local orientation determined. A certain minimum dwell time (of the beam) is needed at each spot for sufficient signal/noise in the EBSD pattern to ensure correct indexing. This time and the size and spatial resolution (step size) of the OIM map determine the total acquisition time. Confidence index (CI) is used to judge the correct indexing of the EBSD patterns obtained. The quality and sharpness of the individual EBSD patterns can also be assessed using the image quality (IQ) parameter. These parameters, amongst others, depends on factors like crystal perfection in the diffraction volume, SEM and OIM system parameters [36, 37], and hence is not an absolute value. For the present study a step size of 3.75 μm was used and the half of a track (from center to the edge of track as shown in Figure 3.5) in the laser dressed sample (1000 W) was selected, covering the whole depth in the resolidified layer. From the x-ray analysis [Section 4.1], the primary phase in the laser-dressed sample was determined to be α-Al_2O_3 and hence the hexagonal crystal structure of alumina was selected to index the EBSD patterns obtained during analysis.

For the OIM analysis the 1000 W laser-dressed sample is used, as at this higher power the depth of the resolidified layer was large enough for it be mounted and polished properly. Although, samples processed under different conditions are used for cooling rate calculations, and for OIM analysis, the change in the processing power has a bearing only on the cooling rate [Section 2.3], and does not affect the solidification behavior. This is because, the microstructures obtained for all the processing powers are very similar in terms of the morphological features present on them and the only change with the increase in laser power is the increase in the depth of the resolidified layer on the surface.

Through a proper polishing protocol, it was possible to obtain good quality EBSD patterns from the alumina ceramic samples. Figure 4.7 shows the comparison of the images obtained from scanning electron imaging and from OIM of the same selected area on the alumina sample. The area selected here is a cross-section of the resolidified layer in one of the tracks.

Only half of the track was selected from center (inset in Figure 3.5) to the edge towards right with proper care that the entire depth of the resolidified layer is mapped for OIM. Such an area was selected as a compromise between the total scan time required for OIM

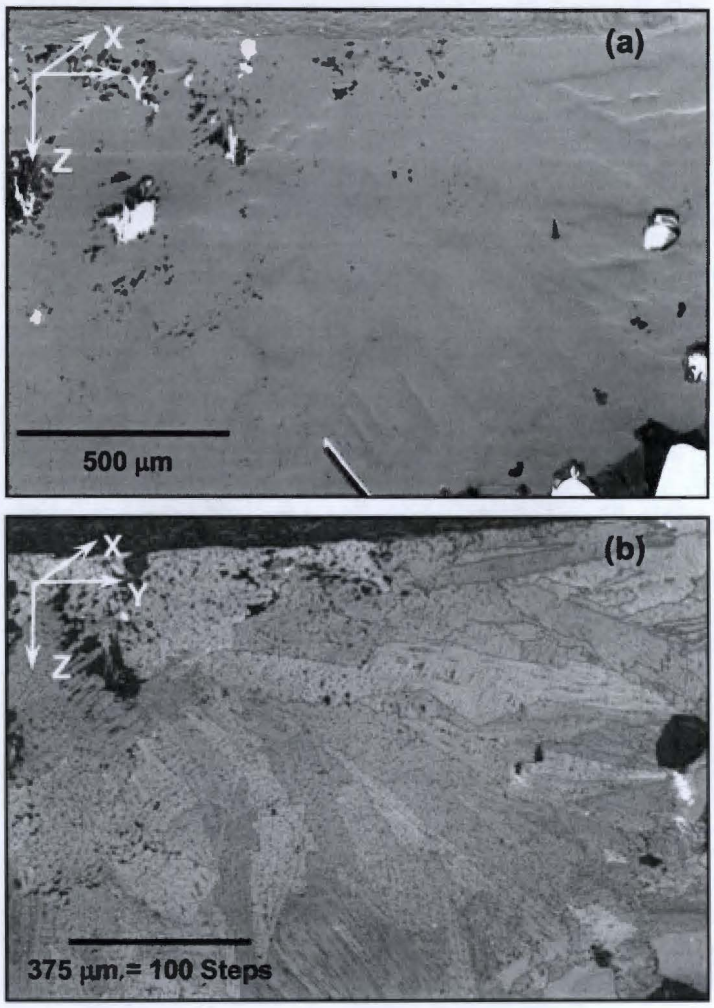

FIGURE 4.7: Low magnification cross-sectional view of the resolidified region within a track of the 1000 W laser-dressed sample. (a) SEM image and (b) image Quality (IQ) image using OIM.

and the pixel spacing that determined the spatial resolution of the OIM maps at this magnification. Figure 4.7a is the secondary electron image of the area and Figure 4.7b is the image quality (IQ) image obtained from OIM. IQ represents the sharpness of the EBSD pattern and thus local crystal perfection and the IQ map reproduces the real microstructure as in conventional scanning or optical microscopy. The completely dark regions in this map are pores, where the value of IQ is essentially zero. Similarly, grain boundaries and other defects are easily detectable as seen in Figure 4.7b. This is in sharp contrast to the secondary electron image of the same area (Figure 4.7a) which does not resolve any grain boundaries at that particular magnification. The growth direction of grains is radial from the free surface at the center of the track where the beam was focused (Figure 4.7b). Figure 4.8 is the Inverse Pole Figure (IPF) map of the same area as in Figure 4.7. In an IPF map, the grains are color-coded for the crystallographic orientation of the local surface normal. The key for the color-coding is given in the stereographic triangle at the bottom. The orientations of selected grains in the figure are shown in the form of the hexagonal cell for α-alumina.

It is very clear from Figure 4.8 that during solidification, growth takes place along the c-axis in the hexagonal α-alumina when subjected to laser irradiation. The grains, like 1-4, have an orientation radially outward from the center of the track as predicted by the heat extraction model [section 3.2]. These are the grains which lie within the resolidified layer. For the grains that are on the surface but away from the center of the track (grain 6 in Figure 4.8), the orientation of cell is parallel to the surface but normal (in Y-direction)

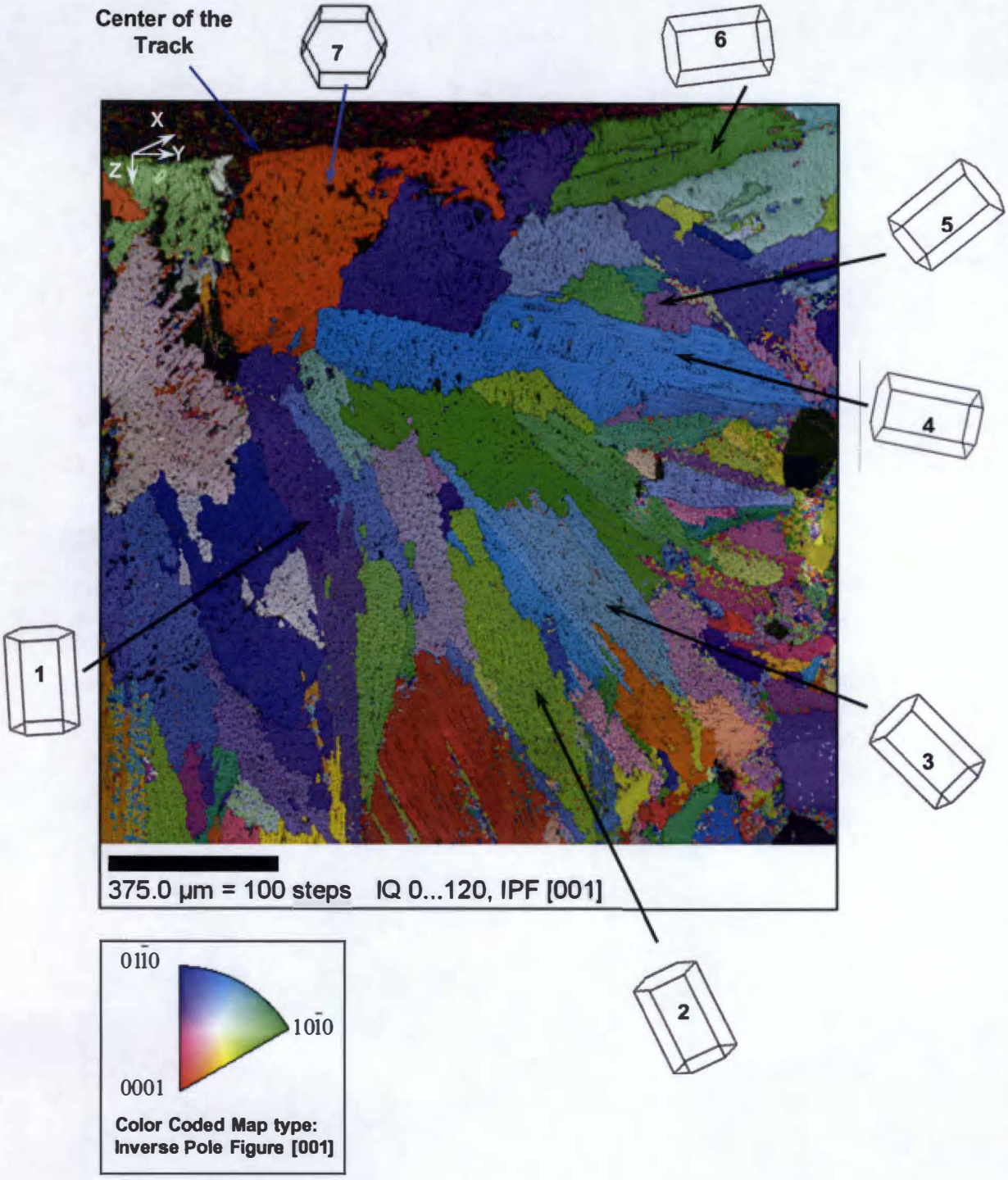

FIGURE 4.8: Inverse Pole Figure (IPF) color-coded map of the selected resolidified area (in cross-section) on the laser-dressed (1000 W) grinding wheel.

to the direction of laser travel (X-direction) in a track. For grain 7, which lies exactly at the center of the track, the cell orientation is along the surface but in a direction opposite to the heat flow. There are some small grains in the resolidified layer (like grain 5) which have their c-axis differently oriented and not along the direction radially outward from the center of the track. It is seen that growth of such grains is suppressed as compared to the others (grains 1-4, 6-7). Thus, a competitive growth mechanism is observed in which growth is very fast for the grains that have their c-axis parallel to the growth direction, where as the growth rate for all other grains is relatively slow. XRD and Pole figure analysis during earlier studies [section 4.1] indicated a preferred orientation for the {110} plane (Figure 4.4). These are the prismatic planes which are parallel to the c-axis in the hexagonal alumina cell. OIM maps suggest that, growth is taking place along the c-axis direction, which would favor {110} planes.

The specific crystallographic texture is expected to provide improved and predictable grinding/machining performance. The next chapter deals with characterizing the functionality of the laser-dressed samples.

5. GRINDABILITY/MACHINABILITY OF LASER-DRESSED WHEELS

Refinement of grain size, densification of surface layer, and evolution of multifaceted grains with cutting edges and vertices are the important morphological modifications taking place on the surface of the wheel due to interaction with laser energy as described in [Section 2.3]. Depending upon the laser processing parameters used, melting (followed by resolidification) and/or vaporization results in this modification of the surface topography (morphology and composition). These morphological modifications are expected to improve cutting efficiency.

5.1 Characterization using Surface Roughness

The morphological features evolved during laser-dressing influence the surface roughness of the dressed wheel, which in turn would affect the grinding performance. Hence, the dressed surface was characterized for surface roughness using stylus-based profilometry.

5.1.1 Stylus Based Roughness Measurement Setup

Surface roughness measurements were done using a stylus-based Mahr Federal Perthometer M1 surface profilometer having a profile resolution of 12 nm. The stylus

tip used was of radius 2 μm with a cone angle of 90°. Some of the salient features of the instrument are:

- Measuring range of up to 150 μm (6000 μin)
- Standards: DIN/ISO/JIS
- Tracing lengths 1.75 mm, 5.6 mm, 17.5 mm (0.7 in, 0.22 in, 0.7 in)
- Cutoff 0.25 mm/0.80 mm/2.5 mm (0.01 in/0.032 in/0.1 in)
- Automatic selection of filter and tracing length conforming to standards
- Phase-corrected profile filter as per DIN EN ISO 11562
- Automatic scaling according to the profile amplitude
- Dynamic pick-up calibration

In the instrument, after carrying out a test measurement, periodic and aperiodic profiles can be identified and the cutoff set, according to standards automatically, such that unintentional non-standard measurements are excluded. The roughness parameters R_a and R_z are calculated as per ISO 4287:1997. For accuracy of the results, five measurements were taken on different parts of the sample surface.

5.1.2 Surface Roughness Profiles

The morphological features evolved during laser-dressing, are expected to influence the surface roughness of the dressed wheel, which in turn would affect the grinding performance. The unfiltered surface roughness profiles for the laser-dressed samples are illustrated in Figure 5.1 and the corresponding surface roughness measurements are

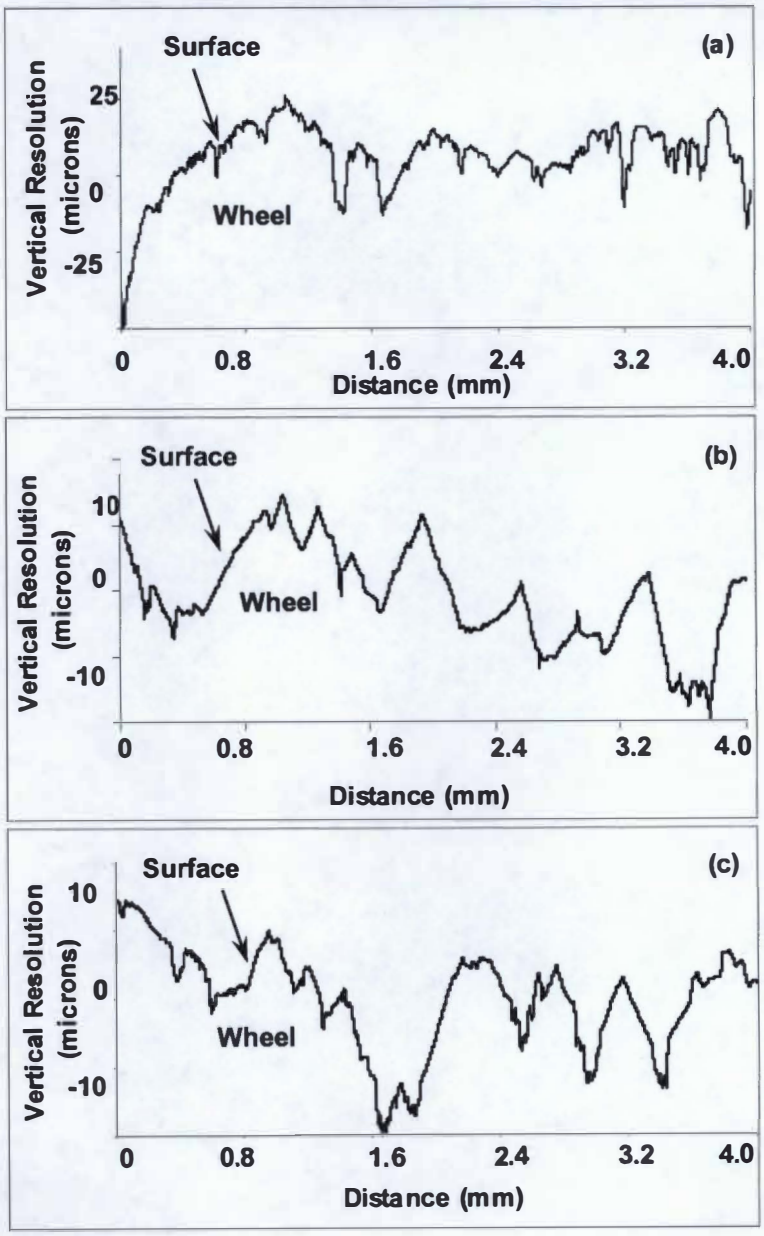

FIGURE 5.1: Unfiltered surface roughness profile of laser-dressed alumina samples for (a) 500 W, (b) 750 W, and (c) 1000 W.

presented in Table 5.1. As the laser power increases there is more melting on the surface and hence greater is the extent and depth of the resolidified layer formed on it. The arithmetic mean roughness (R_a), the average maximum height (R_z) of the profile, and the maximum roughness depth, R_{max} were measured. The Peak Count (RP_c), which gives the number of peaks per length of trace in the profile, is higher for the samples dressed with lower laser power. In general, lower R_a and R_z values combined with a lower RP_c, gives a smoother worksurface finish. From Table 5.1 it can be inferred that, for the samples dressed at higher laser power, the resolidified layer on the top is smoother as compared to the ones processed at lower laser powers. But, the laser power does not have significant effect on the R_a values. Change in the surface roughness will affect the grinding performance of the dressed wheel. To study this, the following section describes a high-speed grinding test.

TABLE 5.1: Surface roughness parameters of the laser-dressed grinding wheel surface.

Laser Power (W)	Ra (μm)	Rz (μm)	Rmax (μm)	RPc (1.0, -1.0) (cm^{-1})
1000	3.554 (±1.7)	20.483	30.966	25
750	2.992 (± 0.71)	15.06	25	26
500	3.454 (± 1.1)	24.02	38.66	38
Undressed sample	The grain size in the sintered wheel is of the order of 100 μm with porosity present in between them.			

5.2 High-Speed Grindability Test

5.2.1 Experimental Details

An in-house built high-speed grinding machine was employed for grinding test of the laser-dressed and undressed samples. The pin-on-disc based high-speed grinding machine (Figure 5.2) comprise of a 3-jaw chuck connected to a servo motor which can rotate at controlled speed (upto 1200 rpm) and torque both clockwise and anti-clockwise. This chuck is used to hold the grinding wheel sample, on which, a pin (AISI 1010 plain carbon steel, 3 mm diameter) is ground. The pin itself can rotate at high speeds ranging from 5000 to 35000 rpm via a high-speed motor that rests on a cantilever arm, above the 3-jaw chuck. To maintain a continuous contact between the pin and the grinding sample during the test, the cantilever beam rests on a compensating spring. The spring tension is adjustable in order to maintain constant zero-load condition on the pin. For the present tests, the grinding wheel sample was kept stationary in between the 3-jaw chuck and the pin was rotated at 15000 rpm for 10 minutes. The end of the pin in contact with the grinding wheel was flat and was prepared on a 180 grit SiC paper to initial surface roughness parameters as described in Table 5.2. The pin was weighed every 2 minutes during the test for weight loss, where as the weight loss in the grinding wheel sample was measured directly after 10 minutes.

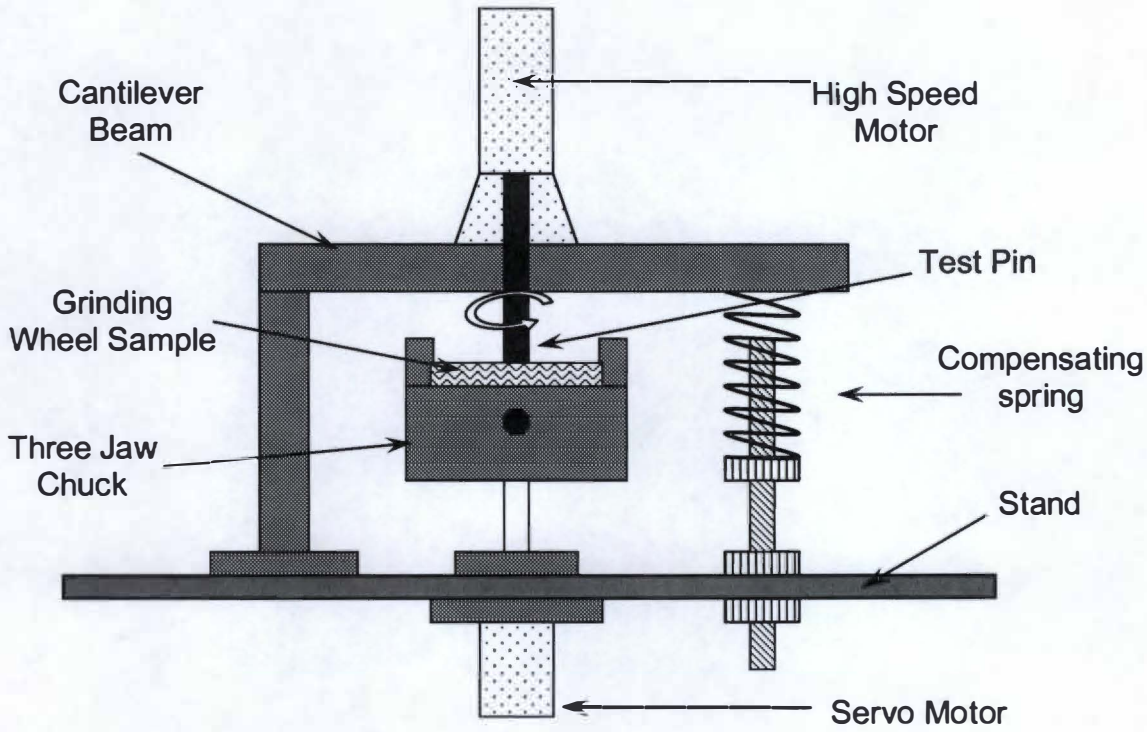

FIGURE 5.2: Schematic of high-speed grinding test apparatus.

TABLE 5.2: Surface roughness parameters of AISI 1010 plain carbon steel prior to high-speed grinding tests.

Sample	Ra (μm)	Rz (μm)	Rmax (μm)	RPc (1.0, -1.0) (cm^{-1})
AISI 1010 plain carbon steel pin prior to high-speed grinding tests	0.2845 (±0.13)	2.0385	2.5285	6

5.2.2 Results and Discussion

Grinding performance was evaluated by grinding of AISI 1010 plain carbon steel pins on the undressed and laser-dressed grinding wheel samples using a high speed grinding machine. The cumulative weight loss in the pins, during grinding is shown in Figure 5.3. For the laser-dressed samples, highest weight loss is seen in the 500 W laser dressed sample. The weight loss in pin ground against the undressed wheel under similar conditions, as that of laser-dressed is very high and also it occurs in a very short time. The grinding test for this sample could not be carried out for the complete ten minutes due to loss of contact between the wheel and pin because of formation of deep groove on the wheel within the first few seconds (~ 20 seconds) of start of test. During this short time there was a very high weight loss in the undressed grinding wheel too, thus reducing the grinding efficiency of the process. The surface roughness profiles produced on the pins after the grinding tests are shown in Figure 5.4 and corresponding surface roughness parameters are given in Table 5.3. For the pin ground against the undressed wheel, the

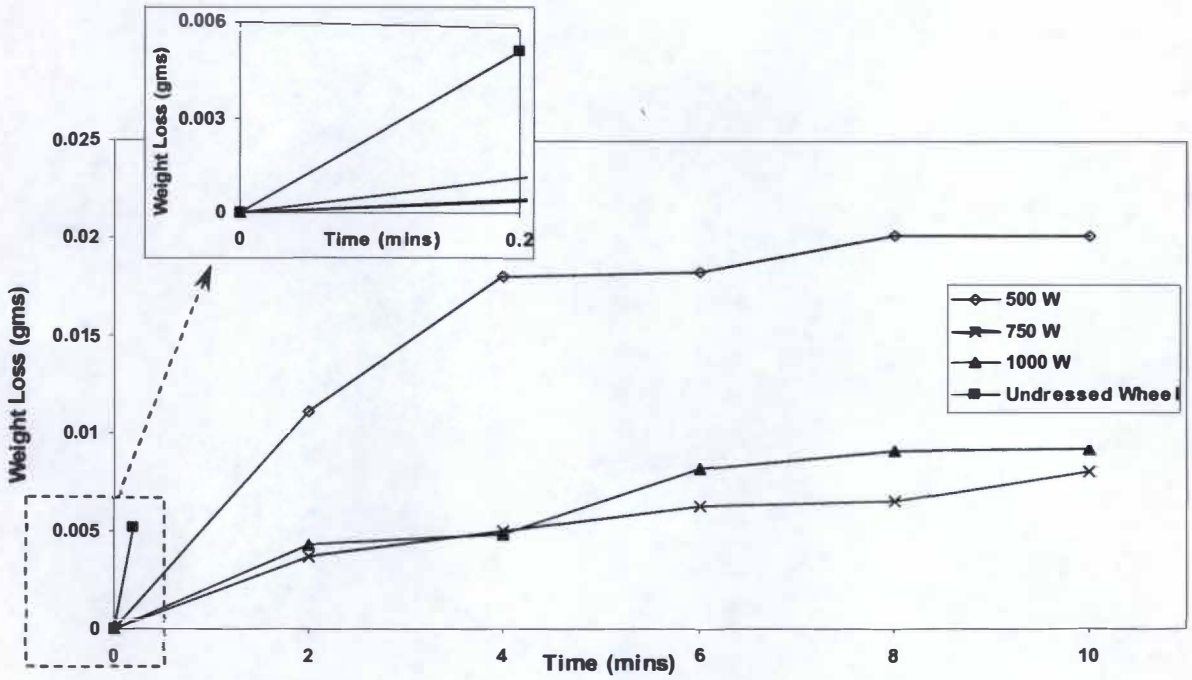

FIGURE 5.3: Cumulative weight loss in the AISI 1010 plain carbon steel pins used for high-speed grinding test of the grinding wheels.

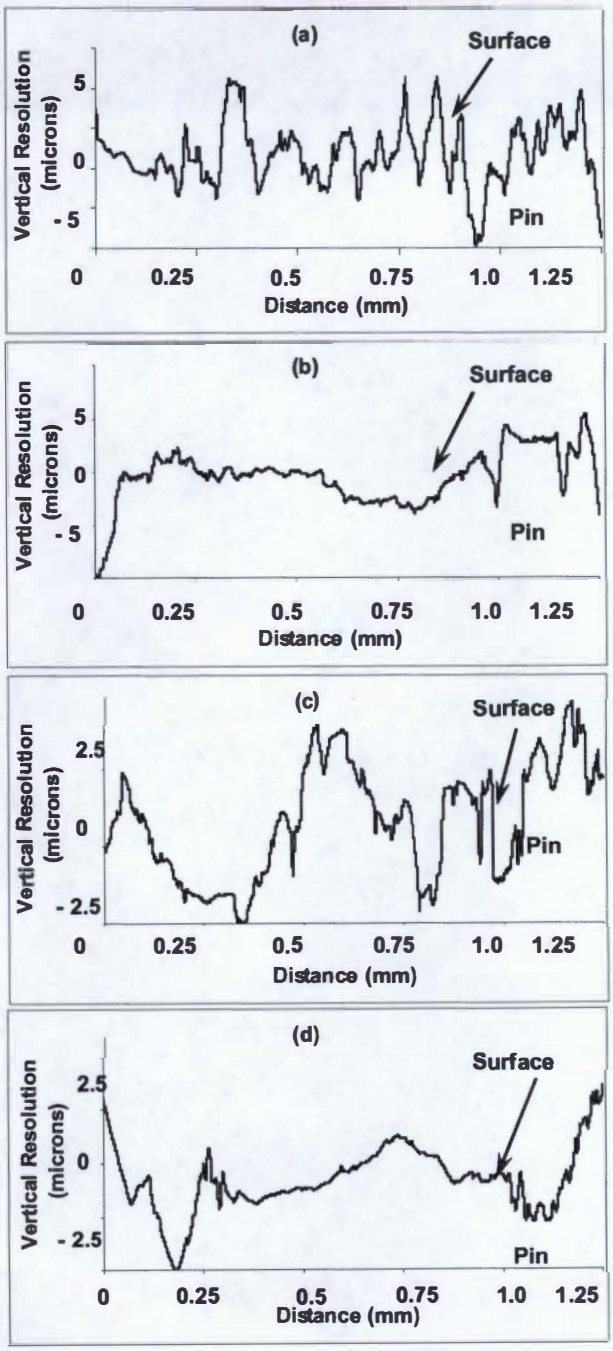

FIGURE 5.4: Unfiltered surface roughness profile of pins used for wear-testing laser-dressed alumina grinding wheels for (a) undressed wheel, (b) 500 W, (c) 750 W, and (d) 1000 W.

TABLE 5.3: Surface roughness parameters of the AISI 1010 plain carbon steel pins after high-speed grinding testing on laser-dressed and undressed grinding wheel surfaces.

Laser Power (W)	Ra (μm)	Rz (μm)	Rmax (μm)	RPc (1.0, -1.0) (cm^{-1})
1000	0.557 (± 0.02)	3.1033	5.38	27
750	0.429 (± 0.11)	2.1566	3.7816	11
500	0.467 (± 0.18)	2.673	6.673	10
Undressed sample	1.859 (±0.21)	10.237	14.2	112

surface roughness parameters are orders of magnitude higher than that for the ones which are ground against the dressed wheel. The smooth surface finish produced on the pin in combination with very low cumulative weight loss in both the pin and dressed grinding wheel; make the laser-dressed grinding wheel surface suitable for microscale grinding process as opposed to the undressed wheel which is more suitable for rough grinding processes. The 750 W laser-dressed sample produced comparatively lower values of roughness parameters (Table 5.1) which resulted in lower weight loss after the grinding test, thus indicating that the processing parameters at this power are suitable for the efficient microscale grinding.

Preliminary attempts were made to understand the grinding behavior of the pins through scanning electron microscopy (SEM) observations. SEM of the worn out pins clearly

revealed the difference in the surface of the pin after grinding test. Higher surface roughness was observed on the pin tested against the undressed wheel (Table 5.3 and Figure 5.5a) compared to when ground against laser-dressed samples. This therefore indicated that in spite of high grinding wheel material loss, undressed sample is more suited for rough and volumetric grinding purposes. On the contrary, for the pins tested against laser-dressed wheels the weight loss in the wheels was negligible (Table 5.4). As it is distinctly clear in SEM observations, the grinding of the steel pins by undressed wheel is dominated by a ploughing mechanism (Figure 5.5a) where as it is predominantly sliding (Figure 5.5b) during grinding by laser-dressed sample. Such distinctly different mechanisms also produced different surface roughness and volume of material removed.

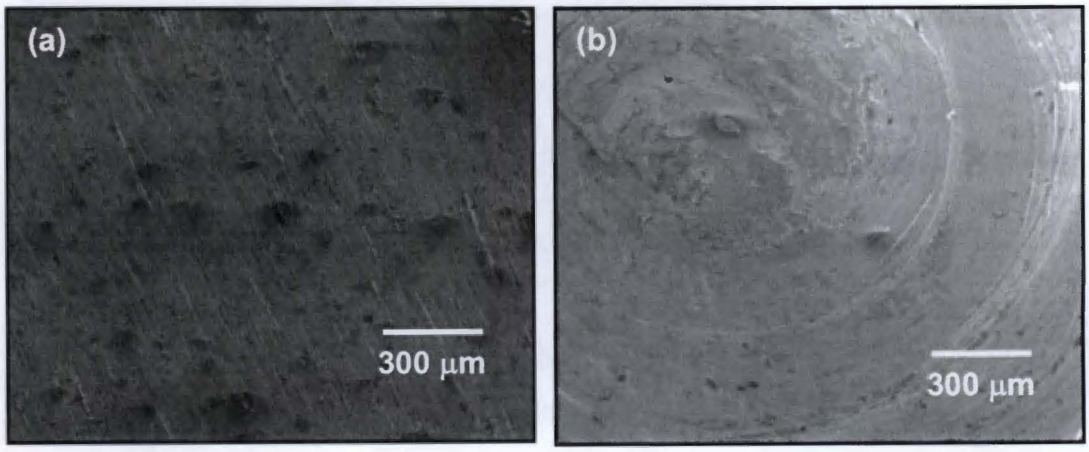

FIGURE 5.5: Surface topography of pins ground against (a) undressed wheel and (b) laser-dressed wheel at 1000 W.

TABLE 5.4: Grinding ratio for high-speed grinding testing of samples laser-dressed at varying laser power.

Sample	Undressed Wheel	Laser-dressed Wheel		
		500 W	750 W	1000 W
Time (minutes)	0.2	10	10	10
Cumulative Weight Loss in Grinding Wheel G (grams/unit contact area)	0.0444	0.0257	0.0203	0.0091
Cumulative Weight Loss in Pin P (grams/unit contact area)	0.00515	0.02017	0.0055	0.00922
Ratio of weight loss in Pin to weight loss in Grinding Wheel: P/G	0.115991	0.784825	0.270936	1.013187

5.2.3 Grinding Efficiency

The effect of surface morphology (crystallographic texture, grain size and roughness) on grinding characteristics can be further realized by evaluating the grinding efficiency of the wheel materials. Such grinding efficiency can be calculated by establishing the ratio of weight loss in the pin to the weight loss in the grinding wheel. Table 5.4 provides numerical values for the grinding efficiency. The weight loss in both pin and wheel are normalized with respect to per unit area of contact in order to directly compare the results. Significantly higher grinding ratio values (> 2 times) of laser-dressed sample in

comparison with undressed samples are indicative of the higher grinding efficiencies with the laser-dressed grinding wheel.

For the 750 W laser-dressed grinding wheel surface roughness values (Table 5.2) are lower than that for 500 W and 1000 W dressed samples. This lower surface roughness value produces smoother surface finish on the ground pin used in grinding test (Table 5.3) although the grinding efficiency is low for the process as compared to wheels dressed at the other two laser powers (Table 5.4). Thus, the surface finish on the workpiece is a direct manifestation of the surface roughness on the wheel and the material removal (wear) mechanism during grinding. The smoother surface finish obtained on the pins ground against laser-dressed grinding wheels in combination with the high grinding ratios obtained from the high-speed grinding test makes the laser-dressed grinding wheel surfaces suitable for high-speed microscale grinding process.

6. CONCLUSIONS

- Refinement in the microstructure is observed after laser-dressing.
- Densification of the surface and the sub-surface structure takes place as a result of reduction in the porosity.
- The particles formed on the surface after dressing are of a specific geometry with multifaceted surfaces having well-defined cutting edges and vertices.
- Particles on the surface developed into preferential orientation after laser-dressing. The (110) plane has preferential orientation in the dressed sample, replacing (116) plane in the undressed condition.
- The high-speed grinding test results show a negligible weight loss in the laser-dressed grinding wheel as compared to the undressed wheel and also higher grinding ratios, making laser-dressing suitable for high-speed microscale grinding.
- Smooth worksurface finish can be obtained using laser-dressed grinding wheel even while maintaining high grinding efficiency.
- Cooling rates of the order of $\sim 10^{2}$°C/sec are observed during the laser-dressing of alumina grinding wheels. For the higher laser power processed samples the cooling rates are lower as compared to that of the samples processed at lower powers.

- In the direction normal to the laser travel, solidification structure changes from equiaxed grains with dendritic structure at the center of track, to columnar near the edges closely following the constitutional supercooling theory.
- OIM analysis shows a preferred growth of grains along the c-axis of the hexagonal alumina cell. This growth is in a direction opposite to that of the heat flow. Further, OIM results in complement with XRD and pole figure analysis, suggests a preferred orientation of grains on the {110} planes, which are parallel to the c-axis in the hexagonal alumina cell.
- A competitive growth mechanism of grains is observed in the resolidified layer, during which the grains with c-axis not oriented radially from the center of the track are suppressed in their growth.

REFERENCES

[1] C. Zhang, Y. C. Shin, "A novel laser-assisted truing and dressing technique for vitrified CBN wheels", *Int. J of Machine Tools & Manufacture,* **42**, 825-835, 2002.

[2] N. Ramesh Babu, V. Radhakrishnan, Y. V. G. S. Murti, "Investigation on Laser-dressing of Grinding Wheels- Part I: Preliminary Study", *J of Engg. For Industry*, **111**, 244-252, 1989.

[3] Mark J. Jackson, B. Mills, "Materials Selection applied to Vitrified Alumina and CBN Grinding Wheels", *J. of Materials Processing Technology*, **108**, 114-124, 2000.

[4] K. Suzuki, T. Uematsu, T. Nakagawa, "On Machine Truing/Dressing of Metal Bond Grinding Wheels By Electro-Discharge of Metal Bond Grinding Wheels By Electro- Machining", *Annals of CIRP,* **36 (1)**,115-118, 1987.

[5] H. Ohmori, T. Nakagawa, "Mirror surface grinding of silicon wafers with electrolytic in-process dressing", *Annals of CIRP,* **39 (1),** 329–332, 1990.

[6] E.S. Lee, "A study on the analysis of grinding mechanism and development of dressing system by using optimum in process electrolytic dressing", *Int. J. Mach. Tools Manufact*, **37**, 1673–1689, 1997.

[7] N. Ramesh Babu, V. Radhakrishnan, "Investigation on Laser-dressing of Grinding Wheels- Part II: Grinding performance of a Laser Dressed Aluminum Oxide Wheel", *J of. Engg. For Industry*, **111,** 253-261, 1989.

[8] X. Chen, W. B. Rowe, B. Mills, D. R. Allanson, "Analysis and Simulation of the Grinding Process. Part III: Comparison with Experiment", *Int. J. Mach. Tools Manufact*, **36 (8),** 897-906, 1996.

[9] T. C. Buttery, A. Statham, and J. B. Perical, "Some effects of dressing on grinding Performance", *Wear*, **55**, 195-219, 1979.

[10] Richard P. Feynman: "The Feynman Lectures on Physics", Addison-Wesley Publication Company, Menlo Park, CA, 1986.

[11] N. Ramesh Babu, V. Radhakrishnan, "Influence of Dressing Feed on the performance of Laser Dressed Al_2O_3 wheel in wet grinding", *Int. J. Mach. Tools Manufact,* **35,** 661-671,1995.

[12] K. Jodan, H. Funakoshi, K. Matsumara, K. Ishizaki , "Laser-dressing process of porous cast-iron bonded diamond grinding wheels for machining ceramics", *Adv. In Tech. of Mat. Proc. J. (ATM),* **2 (2),** 117-123, 2000.

[13] K. Jodan, K. Matsumara, K. Ishizaki, "Low specific-grinding energy machining of ceramics by a laser dressed diamond grinding stone", *Adv. In Tech. of Mat. Proc. J. (ATM)*, **5 (2),** 40-45, 2003.

[14] J. Lawrence, L. Li, J. T. Spencer, "The effects of high-power diode laser radiation on the wettability, adhesion and bonding characteristics of an alumina/silica-based oxide and vitreous enamel", *Surface and Coatings Technology*, **115,** 273-281, 1999.

15 Y. Yuanzheng, Z. Youlan, L. Zhengyi, C. Yuzhi, "Laser remelting of plasma sprayed Al_2O_3 ceramic coatings and subsequent wear resistance", *Materials Science and Engineering A*, **291,** 168-172, 2000.

16 L. Bradley, L. Li, F. H. Stott, "Flame-assisted laser surface treatment of refractory materials for crack-free densification", *Materials Science and Engineering A*, **278,** 204-212, 2000.

17 J. Lawrence, L. Li, "Surface treatment of an Al_2O_3-based refractory with CO_2 and high power diode laser for improved mechanical and chemical resistance characteristics", *Surface and Coatings Technology*, **162,** 93-100, 2002.

18 D. A. Porter, K. E. Easterling, "Phase Transformation in Metals and Alloys", Second Edition, 214-222.

19 J. Lawrence, L. Li, J. T. Spencer, "The effects of high-power diode laser radiation on the wettability, adhesion and bonding characteristics of an alumina/silica-based oxide and vitreous enamel", *Surface and Coatings Technology*, **115**, 273-281, 1999.

20 D. Triantafyllidis, L. Li, F. H. Stott, "Surface treatment of alumina-based ceramic using combined laser sources" *Appl. Surface Science*, **186**, 140-144, 2002.

21 W. Kurz, R. Trivedi, Trans. *ASME*, **114**, 450, 1992.

22 A. Kar, J. Mazumdar, J App Physics, **61**, 2645, 1987.

23 M. Rappaz, S. David, J. M. Vitek, L. A. Boatner, *Metall. Trans. A.,* **20A**, 1125, 1989.

24 J. Mazumdar, W. M. Steen, , *J. Appl. Phys.*, **51(2),** 941-947, 1980.

[25] M. C. Fleming, "Solidification Processing", McGraw Hill, NY, 1974.

[26] O. Esquivel, J. Mazumdar, M. Bass, S. M. Copeley, "Microstructural formation according to the theory of constitutional supercooling". In: R. Mehrabian, B. H. Kear, M. Cohen, editors. "Rapid solidification processing, principles and technologies" II. Baton Rouge: Claitors, 150-73, 1980.

[27] D. Rosenthal, *Welding Journal*, **20**, 220-234, 1941.

[28] D. Rosenthal, *Trans Amer. Soc. Mech. Engg*, **68**, 849, 1946.

[29] H.S. Carslaw and J.C. Jaeger, *Conduction of Heat in Solids* (Oxford: Clarendon Press, Oxford, 1962).

[30] S. Kou and R. Mehrabian, editors: Modeling of Casting and Welding Processes III (The Metals, Minerals and Materials Society, TMS, Warrendale, PA, 1986).

[31] D. Bäuerle, "Laser Processing and Chemistry" (3rd ed., Springer, Berlin, 68-176, 2000).

[32] D.J. Dingley, V. Randle, J Mater Science, **27**, 4585, 1992.

[33] D. J. Dingley, D. P. Field, *Mat Sci Technology*, **12 (1),** 1996.

[34] D. P. Field, *Ultramicroscopy*, **67 (1),** 1997.

[35] B. K. Kim, J. A. Szpunar, *Scripta Materialia*, **44**, 2605, 2001.

[36] J. K. Farrer, J. R. Michael, C. B. Carter, in: A. J. Schwartz, M. Kumar, B. L. Adams (Eds.), Electron Backscatter Diffraction in Material Science, Kluwer Academic/Plenum Publishers, NY, 299, 2000.

[37] K. Z. Baba-Kishi, *J. Mat. Sci.,* **37**, 1715, 2002.

[38] P. Gilormini, E. Felder, "Theoretical and experimental study of the ploughing of a rigid-plastic semi-infinite body by a rigid pyramidal indenter", *Wear,* **88**, 195–206, 1983.

[39] J.A. Williams, Y. Xie, "The generation of wear surfaces by the interaction of parallel grooves", Wear, **155**, 363–379, 1992.

[40] Y. Xie, J.A. Williams, "The prediction of friction and wear when a soft surface slides against a hard rough surface", *Wear,* **196,** 21–34, 1996.

[41] A.A. Torrance, J.A. Badger, "The relation between the traverse dressing of vitrified grinding wheels and their performance", *Int. J of Machine Tools & Manufacture*, **40**, 1787–1811, 2000.

APPENDIX

A-1: Metal Removal Model for Laser Dressed Grinding Wheels

The laser-dressed grinding wheels develop particles with cutting edges and vertices [section 2.3]. These particles with specific geometries will have an effect on the metal removal rate during the grinding process. The abrasive particles can be idealized as pyramidal indenters, based on the shape of the grains formed after laser-dressing (Figure A.1), to calculate metal removal rates during the grinding process. The proposed model assumes simultaneous ploughing and cutting by the grit, where ploughing is the sideways flow of material round the indenter [38]. Including rubbing action as well in the model, which is the flow and deformation of metal beneath the indenter, amount of cutting can be predicted [39]. Relationship for force ratio (μ) and abrasive wear ratio (K) can be given by [40]:

$$\mu \approx \left(\frac{1.382}{l^{0.25}}\right)\left[1 - 1.23\,\mu_o\right] \qquad [A.1]$$

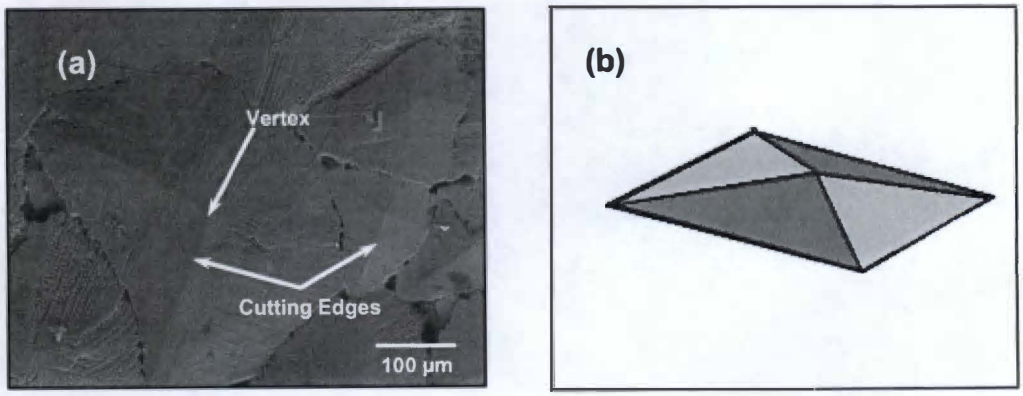

FIGURE A.1: (a) Laser-dressed grinding wheel showing pyramidal grains (grits), and (b) approximation of the grit as a pyramidal indenter.

for attack angles (α) equal to or greater than 60°. μ_o is the coefficient of friction on the grit rake interface.

and,

$$K \approx \frac{0.003}{\mu_o \kappa l^{0.5}} \left(\frac{H_b}{H_s} \right)^{0.5} \qquad [A.2]$$

for attack angles equal to or greater than 45°.

The attack angles for grains formed after laser-dressing, as seen from Figure A.1, are more than 60°, for the above equations to be valid. Using wear equation, the metal removal rate per grit *(Z_g) is* given by [41]:

$$Z_g = K \cdot f_n \cdot V_s = K \cdot V_s \cdot \left(\frac{d}{\tan \alpha} \right)^2 H_s \qquad [A.3]$$

where, V_s is the grinding wheel speed. If the geometry of the arc of cut is l_a and there are n_g grits per unit area in contact, then the specific metal removal rate (Z') for the wheel is given by [41]:

$$Z' = K \cdot V_s \cdot \left(\frac{d}{\tan \alpha} \right)^2 H_s \cdot l_a \cdot n_g \qquad [A.4]$$

Calculation of specific metal removal rates by the above model requires an experimental setup simulating the actual grinding operation with measurement of parameters like coefficient of friction and forces. This was beyond the scope of the work carried out so far and definitely needs to be dealt with in future.

VITA

Abhijeet A. Khangar was born on 30th August 1980 in Nagpur, India. He completed his Bachelor of Engineering Degree in Metallurgical Engineering from Visvesvaraya National Institute of Technology, Nagpur, India in 2002. He then enrolled for the Master of Science degree with Materials Science and Engineering as major at the University of Tennessee-Knoxville (UTK) in August 2002. He worked at UTK as a Graduate Research Assistant with Prof. Narendra B. Dahotre. His dissertation topic during this study was "Laser-Dressing of Alumina for Grinding Wheels". For completion of part of the research work, he also worked at Oak Ridge National Lab, TN, USA. He has written several referred journal papers on the topic.